MSC-07230
SUPPLEMENT 1

NATIONAL AERONAUTICS AND SPACE ADMINISTRATION

# APOLLO 16 MISSION REPORT

## SUPPLEMENT 1

# APOLLO 16 GUIDANCE, NAVIGATION, AND CONTROL SYSTEM PERFORMANCE ANALYSIS REPORT



MANNED SPACECRAFT CENTER
HOUSTON, TEXAS
OCTOBER 1972

MSC-07230

# APOLLO 16 MISSION REPORT

## SUPPLEMENT 1

# APOLLO 16 GUIDANCE, NAVIGATION, AND CONTROL SYSTEM PERFORMANCE ANALYSIS REPORT

PREPARED BY

TRW Systems

APPROVED BY

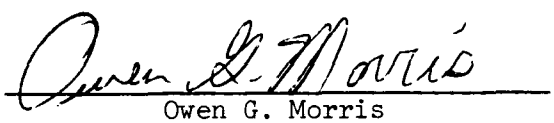

Owen G. Morris
Manager, Apollo Spacecraft Program

NATIONAL AERONAUTICS AND SPACE ADMINISTRATION
MANNED SPACECRAFT CENTER
HOUSTON, TEXAS
OCTOBER 1972

PROJECT TECHNICAL REPORT

TASK E-38F

# APOLLO 16 GUIDANCE, NAVIGATION, AND CONTROL SYSTEM PERFORMANCE ANALYSIS REPORT

NAS 9-12330

30 AUGUST 1972

Prepared for
NATIONAL AERONAUTICS AND SPACE ADMINISTRATION
MANNED SPACECRAFT CENTER
HOUSTON, TEXAS

Prepared by
Electronic Systems
Engineering Department

PROJECT TECHNICAL REPORT
TASK E-38F

# APOLLO 16 GUIDANCE, NAVIGATION, AND CONTROL SYSTEM PERFORMANCE ANALYSIS REPORT

NAS 9-12330

30 AUGUST 1972

Prepared for
NATIONAL AERONAUTICS AND SPACE ADMINISTRATION
MANNED SPACECRAFT CENTER
HOUSTON, TEXAS

Prepared by
Electronic Systems
Engineering Department

Approved by _____
J. E. Alexander, Manager
Electronic Systems Engineering
Department

Approved by _____
D. L. Rue, Manager
Task E-38F

TABLE OF CONTENTS

# TABLES

ILLUSTRATIONS

## NOMENCLATURE

| | |
|---|---|
| ACB (X, Y, Z) | Accelerometer bias (Channels X, Y, Z) |
| ADSRA (X, Y, Z) | Gyro drift due to acceleration along the spin reference axis (Channels X, Y, Z) |
| ADIA (X, Y, Z) | Gyro drift due to acceleration along the input axis (Channels X, Y, Z) |
| AGS | Abort Guidance System |
| AOT | Alignment Optical Telescope |
| APS | Ascent Propulsion System |
| ASA | Abort Sensor Assembly |
| CDU | Coupling Data Unit |
| CM | Command Module |
| CMC | Command Module Computer |
| DAP | Digital Autopilot |
| DC | Direction Cosine |
| DPS | Descent Propulsion System |
| DSKY | Display and Keyboard |
| EMS | Entry Monitor System |
| EPC | Earth Prelaunch Calibration |
| FDAI | Flight Director Attitude Indicator |
| GDA | Gimbal Drive Actuator |
| GET | Ground Elapsed Time (Range Time) |
| GN&C | Guidance, Navigation and Control |
| IFC | Inflight Calibration |
| IMU | Inertial Measurement Unit |
| IRIG | Inertial Rate Integrating Gyro |
| LGC | LM Guidance Computer |
| LM | Lunar Module |
| LR | Landing Radar |
| MERU | Milli-Earth Rotational Units |
| MIT/CSDL | MIT/Charles Stark Draper Laboratory |
| MSC | Manned Spacecraft Center |

| | |
|---|---|
| MSFN | Manned Space Flight Network |
| NASA | National Aeronautics and Space Administration |
| NAV BASE | Navigation Base |
| NBD (X, Y, Z) | Gyro Bias Drift |
| ORB RATE | Orbital Rate |
| PDI | Powered Descent Initiation |
| PGNCS | Primary Guidance, Navigation and Control System |
| PIC | Pre-installation Calibration |
| PIPA | Pulsed Integrating Pendulous Accelerometer |
| PPM | Parts per Million |
| RCS | Reaction Control System |
| RSS | Root of the Sum of the Squares |
| S/C | Spacecraft |
| SCT | Scanning Telescope |
| SFE (X, Y, Z) | PIPA Scale Factor (Channels X, Y, Z) |
| SM | Service Module |
| SPS | Service Propulsion System |
| SIMBAY | Scientific Instrumentation Module Bay |
| TEI | Trans-Earth Insertion |

# 1.0 INTRODUCTION

## 1.1 GENERAL

This report presents conclusions and results from the detailed analysis of Apollo 16 Guidance, Navigation and Control equipment inflight performance. The analysis results will supplement discussions of Command and Service Module and Lunar Module GN&C performance presented in the Apollo 16 Mission Report (Reference 1).

# 2.0 SUMMARY

Included herein are the results of additional studies which were conducted to supplement conclusions drawn in the MSC Mission Report and analyses which were not completed in time to meet the Mission Report deadline. Section 3 contains a detailed evaluation of the Abort Guidance System sensor assembly and contains results from the investigation of the X gyro loop anomaly. Section 4 presents further evidence substantiating the excellent LM IMU performance obtained from preliminary indications. Section 5 presents a detailed study of the procedural changes implemented on Apollo 16 to diminish the number and duration of interruptions to the CSM DAP attitude maneuver during P20 Option 5 operations. Summaries of the Sections 3, 4 and 5 results are presented in the following paragraphs.

A problem in the X gyro loop of the AGS attitude reference system caused a gradual build-up in cross-range velocity error during descent which grew to approximately 28 feet per second at the time of touchdown. The other two axes, vertical and downrange velocity, were virtually unaffected and the AGS provided excellent altitude and altitude rate reference data to the astronauts during descent. Exact cause for the X gyro loop anomaly is not determinable from available telemetry data. The two most probable candidates for the cause are (1) bubble or contamination between the X gyro sensitive element and case or (2) a pulse torque servo amplifier electronics intermittent error. Numerous failure mechanisms were hypothesized by the sensor assembly manufacturer; however, no one hypothesis fits all the observed flight data and Abort Sensor Assembly test history. Review of preflight data from the anomalous gyro yielded no suspicious areas and provided no correlation to previously known gyro failure modes. Gyro settling tests have been performed on all field ASA's to screen for gyro fluid bubbles and contamination. Additional settling tests will be performed on the Apollo 17 ASA, approximately 90 days before launch, preceding its installation in the LM.

LM IMU performance throughout the mission was excellent. Comparisons of a navigated state velocity using only IMU data with best estimate end

point conditions at touchdown and at ascent insertion indicated that the IMU misalignments and accelerometer bias errors were less than the preflight one sigma uncertainties.

Several procedural changes and DAP erasable load changes were implemented for the Apollo 16 mission to alleviate pointing error and extraneous RCS jet firing problems detected on Apollo 15. CSM DAP analysis of the P20 Option 5 attitude pointing verified that the changes adopted for this mission corrected the problems for the CSM/LM docked configuration and significantly reduced the number of RCS firings. In the CSM-alone configuration, 2.5 and 3.0 degree deadbands were tested as replacements for the 5.0 degree deadband used on Apollo 15 for the purpose of reducing average pointing error. Observed DAP performance for the CSM-alone configuration agreed closely with preflight simulations except the flight data could not substantiate that the 2.5 degree deadband provided tighter pointing. Apparently disturbance torques resulting from uncontrolled venting offset the advantages of the 2.5 degree deadband over the slightly larger 3.0 deadband.

# 3.0 AGS

## 3.1 FUNCTIONAL PERFORMANCE

The AGS remained in the monitor mode during descent, ascent and rendezvous and provided sufficient data to establish the integrity of the primary system. Pre-PDI system power-up, calibration, state vector transfer and AGS to PGNCS alignment were accomplished without incident. Accelerometer bias and gyro drift shifts from the prelaunch calibration were easily within limits giving no indication of degraded instrument performance since the time of the prelaunch calibration. Because of the nominal PDI waive-off the state vector transfer and AGS to PGNCS align were performed again approximately 5 hours later. Misalignments between AGS and PGNCS at time of PDI, which occurred approximately 8 minutes after the alignment, were all less than 0.03 degrees. Immediately after PDI, the real-time velocity differences between AGS and PGNCS showed a rapid divergence in the out-of-plane Y channel. AGS minus powered flight processor differences showed a similar trend thus isolating the cause to AGS. Real-time AGS minus PGNCS velocity differences reflect total state vector differences and contain the effects of landing radar updating. In order to completely eliminate the landing radar contributions, postflight velocity comparisons were derived using only the inertial sensed velocity outputs from each system and are shown in Figures 3-1 through 3-3. As shown in Figure 3-2 the postflight comparison confirms the real-time results and reflects a misalignment type error source since the velocity errors in the other two channels are comparatively small. Further real-time evidence of a misalignment error was the observed difference between AGS and PGNCS inertial attitude at touchdown of 0.46 degrees. Detailed postflight analysis has shown that 0.26 degrees of the Z misalignment was accumulated in the first 100 seconds after PDI and the remaining error was accumulated gradually over the remainder of the burn as the result of X gyro drift. Due to the attitude of the spacecraft at PDI, some of the large misalignment which was accumulated during the first 100 seconds coupled into the inertial X axis. Using Z and X inertial misalignments (IMZ and IMX) accumulated immediately after PDI, the observed subsequent X gyro drift (XGB) and the appropriate error

partial derivatives, the following Y inertial axis end point velocity error was predicted:

| Error Source $\epsilon_i$ | Measured Value | $\partial\Delta V_y/\partial\epsilon_i$ (1) | (PGNCS-AGS) $\Delta Vy$ |
|---|---|---|---|
| IMX | 383 arc sec | 0.027 fps/sec | 10.34 |
| IMZ | 926 arc sec | 0.011 fps/sec | 10.19 |
| XGB | 1.94 deg/hr | 4.5 fps/deg/hr | 8.7 |
| | | TOTAL ERROR = | 29.23 fps |

Figure 3-2 shows an end point error of 28.8 fps, establishing that the velocity error was caused by the misalignments and the gyro drift observed. Detailed analysis has shown that the large inertial misalignments which developed immediately after PDI were caused by a rapidly building X gyro loop error. For the remainder of the mission, X gyro loop bias continued to exhibit instability and apparent "g" sensitive or "g" induced drift was evident. Detailed analysis of the other two gyros and possible causes for the X gyro loop problem are presented in Section 3.2.2. Figures 3-1 and 3-3, X and Z inertial velocity differences are small and typical of differences observed on previous missions. Cause for the 3 ft/sec difference in X appears to be partially PGNCS, because the AGS required an X velocity update of less than 0.5 ft/sec at 104:26:30 AET when the PGNCS radar supplemented X velocity was loaded into the AGS computer. Some of the X and Z difference resulted from AGS accelerometer error and accelerometer performance for descent and ascent is presented in Section 3.2.2.

## 3.2 SENSOR PERFORMANCE

### 3.2.1 Gyro and Accelerometer Free-Flight Performance

AGS accelerometer biases determined from calibrations and free-flight velocity accumulations are shown in Table 3.1. The histories show good long and short term stability.

(1) The effects of IMX, IMY and XGB on $\Delta V_x$ and $\Delta V_z$ are second order.

Preflight calibrations, inflight calibrations and AGS/PGNCS attitude comparisons during coasting flight yielded the gyro static bias estimates shown in Table 3.2. The Y and Z gyro bias variations are within allowable limits and are representative of data obtained from previous missions. The X gyro variations before descent were small. However, the bias thereafter, based on the data observed during free-flight post ascent, was erratic and not representative of normal gyro operation. The problem which caused the rapidly building X gyro loop error immediately after PDI apparently had some effect on the X gyro loop bias stability.

### 3.2.2 AGS-PGNCS Attitude Differences During Powered Flight

Gyro error estimates for Apollo 16 were derived from two data sources; 1) body angle differences which are the small angle differences between the AGS direction cosine matrix and the PGNCS gimbal angle matrix and 2) integrated body rate differences which are computed based on the changes observed in the previously mentioned AGS and PGNCS matrices. The first set of differences will be referred to as delta theta angles ($\Delta\theta$) and the second set will be called delta omega differences ($\Delta\Omega$). Delta theta differences contain the initial misalignment and the error propagation effects as the result of misalignments and body maneuvers, as well as the gyro drift effects. Delta omega differences are more direct measures of gyro drift since they do not contain the misalignment effects. However, the delta omega differences are most susceptible to data processing problems resulting from poor quality telemetry data and can present misleading results. In the following presentation, conclusions will be drawn only when the delta theta differences substantiate the delta omega results.

#### 3.2.2.1 Descent Attitude Differences

Two sets of data plots are provided to support the descent analysis.

1) $\Delta\theta$: AGS-PGNCS body angle differences (Figures 3-4 through 3-6).

2) $\Delta\Omega$: AGS-PGNCS integrated body rate difference (Figures 3-7 through 3-9).

The reference time for each plot is 104:17:00.61 (LGC clock time) which is approximately 25 seconds before PDI. Figures 3-4 and 3-6 show the rapidly building error in X and Z for the first 100 seconds after PDI. For the remainder of descent, the delta theta X rate is primarily the result of the gyro loop drift and the delta theta Z rate is primarily the result of the X misalignment which exists and the body rate about Y. Error models developed for the Z body difference during descent verified that the Z body difference could be accounted for with the X misalignment, X gyro drift and Y body rates observed. Figures 3-7 and 3-9, the integrated body rate differences for X and Z, which contain primarily gyro drift effects, confirm this conclusion and show the X gyro drifting at approximately 1.94 deg/hr after the initial high drift rate ceases and negligible drift in the Z channel. Correlation of the observed drift with acceleration is evident in Figure 3-10 where X body axis acceleration and body angle difference are presented on the same plot. When throttle recovery occurs (TR) for example, a noticeable flattening of the error build-up is observable. Using the slope measureable from Figures 3-7 through 3-9 and the residual static drifts recoverable from Table 3.2, the following set of gyro errors is formulated:

| Error Term | Value | Source |
|---|---|---|
| X gyro fixed drift | 0.07°/hr | Table 3.2 [col.(3) -(2)] |
| X gyro spin axis mass unbalance | 5.2°/hr/g | Figure 3-7 $\left[\frac{1.94-0.07}{0.36\ g}\right]$ where 0.36g=avg. accel. |
| Y gyro fixed drift | -0.06°/hr | Table 3.2 [col.(3) -(2)] |
| Y gyro dynamic drift | -0.37°/hr | Figure 3-8 [-0.43 -(0.06] |
| Z gyro fixed drift | -0.16°/hr | Table 3.2 [col.(3) -(2)] |
| Z gyro dynamic drift | 0.08°/hr | Figure 3-9 [-0.08 -(-0.16)] |

### 3.2.2.2 Ascent Attitude Differences

For ascent, the body angle differences provide the primary information on gyro errors, and are presented in Figures 3-11 through 3-13. The noticeable difference between ascent data and descent was the absence of the rapid error build-up at ignition in the X body attitude error. However, the X body angle difference does reflect an attitude error build-up throughout ascent which terminates at insertion again providing strong indication of a "g" sensitive error. A review of Z body angle difference shows a similar error building throughout ascent which is associated with the building X attitude error and Y body rate present throughout ascent. For example, error modeling of the X and Z body angle differences during ascent showed that 6.78 deg/hr/g X gyro mass unbalance along the spin reference axis (XMUSRA) error would fit both X and Z observed body angle differences and the modeled errors are presented as dashed lines on Figures 3-11 and 3-13. Figure 3-14, X Integrated Body Rate Difference, which primarily reflects net gyro drift shows an average slope of 3.25 deg/hr and correlates with the MUSRA value since the average acceleration during ascent is 0.47 g's (3.25 ÷ 0.47 = 6.9 deg/hr/g). Delta omega differences for the Y and Z channels were not included due to postflight data processing problems. However, absence of these data were not critical for ascent because of the clear reflection of Y and Z gyro errors in the delta theta differences. If the 3.25 deg/hr is now accepted as reasonable representation of the X gyro net residual drift, a breakdown of this drift into static and dynamic error follows:

#### Static Error

Static error is most readily observable after orbit insertion by monitoring the residual drift. Residual error is by definition equal to static drift plus compensation where compensation is loaded into the AGS computer as the negative of the observed drift during a calibration. On the surface, the calibration yielded a value of 1.13 deg/hr. This value is believed to contain some "g" sensitive error, however, for simplicity this analysis will consider the effects of the 1.13 compensation on the residual static drift and the g sensitive drift will be handled separately. After orbit insertion, body angle difference data showed a residual drift in the X direction which varied from -1.58 to -0.36 deg/hr. This yields a static drift varying from -0.45 to 0.77 deg/hr.

Dynamic Error

As was the case during descent, most of the observed dynamic error has strong indications of being "g" sensitive error and is estimated based on the following equation.

observed net drift = residual static drift + dynamic drift

The observed net drift was 3.25 deg/hr minus the residual drift range (-1.58 to -0.36) yielding a range of dynamic error of 4.83 to 3.61 deg/hr. Considering an average "g" level of 0.47 for ascent, the X gyro MUSRA term for ascent is estimated to be 10.2 deg/hr/g to 7.7 deg/hr/g.

Since most of the Z body attitude error can be explained as a result of the X attitude errors and Y body rate, the estimate of the Z gyro dynamic error is zero. For the Y channel, Figure 3-12 shows a trend of -0.48 deg/hr and is totally dynamic error since no static error was observable after insertion. For ascent, all of the estimated gyro errors are summarized as follows:

| Error Term | Value | Data Source |
|---|---|---|
| X gyro fixed drift | -0.45 to 0.77 deg/hr | See discussion above |
| X gyro spin axis mass unbalance | 10.2 to 7.7 deg/hr/g | See discussion above |
| Y gyro fixed drift | 0 | Table 3.2 [col.(5) -col. (4)] |
| Y gyro dynamic drift | -0.48 deg/hr | Figure 3-12 |
| Z gyro fixed drift | 0 | Table 3.2 [col.(5) -col.(4)] |
| Z gyro dynamic drift | 0 | See discussion above |

3.2.2.3 X Gyro Loop Anomaly

Figure 3-15 relates the overall mission performance characteristics of the X gyro loop on Apollo 16 in terms of g sensitive and static drift. The gyro was clearly functioning properly before PDI which implies that the problem is g sensitive or the problem is an intermittent type of failure in the presence of acceleration. Figure 3-15 also shows that some instability remained in the gyro loop for the remainder of the mission after PDI. Two gyro loop error mechanisms; (1) X gyro spin axis mass unbalance, and (2) a pulse torquer servo amplifier (PTSA) electronics intermittent error, were considered the two most probable candidates. Other failure mechanisms such as software anomalies, magnetic fields, power supply variations, spin

motor speed variations and wiring problems were investigated and eliminated. The first candidate, an X-gyro spin axis mass unbalance shift, explains the majority of the data (i.e., between PDI + 90 seconds and post-ascent when the system returns to zero "g") showing a persistent 7-10 deg/hr/g of mass unbalance. Several gyro failure modes could be suggested which would exhibit this level of anomalous performance; however, the gyro performance in the early seconds of descent is extremely difficult to explain in terms of a g sensitive gyro error due to the huge size of the drift (requires very large torques) and the speed at which the drift changes (drift rates which are "g" sensitive usually change slowly). The second candidate, failure in the PTSA is predicated on the theory that a bad connection exists on an electronic component and the presence of acceleration and vibration causes this connection to make and break intermittently. Detailed analysis of the failure modes speculated for each of the two candidates are presented in the following paragraphs.

X Gyro Spin Axis Mass Unbalance Instability

A cross-section of the gyro type used on Apollo 16 is shown in Figure 3-16. The manufacturer hypothesized many of the probable failure mechanisms within the gyro and computed the potential torques associated with each failure mechanism.[1] The second consideration was, if the gyro failed in the manner speculated could it recover to the level of performance observed for the remainder of the mission? The major gyro components and the speculated part failures considered are listed in Table 3.3. The table shows only five possible causes which fit the anomaly:

1) Stator assembly shaft movement.
2) Damping fluid inside the inner float.
3) A particle or bubble between the outer float and case.
4) Broken pivot on outer float.
5) Cracked pivot support for outer float (jewel and/or endstone)

The first item has very low probability. For the shaft to move, both pillar blocks (see Figure 3-16) must loosen. There is no history of this happening with the type gyro used in ASA 013. The second item, fluid in the float,

[1] A detailed analysis of the anomaly was conducted by Hamilton Standard System Center and is presented in HSSC report, "ASA 013 Data Review and Explanation of Apparent X Gyro Loop Drift Rate Change," dated 30 June 1972.

would require fluid to leak into the float sometime after the last pre-launch calibration, and then spread out after the application of thrust at PDI. Again there is no history of fluid leakage into the float for the gyro type used on this mission. Item 3, a particle resulting from contamination or a bubble which suddenly emerged is possible; however, it is likely that such a problem would have shown up in the long test history for this particular gyro (approximately 2 years). Items 4 and 5 are highly improbable, because performance would be expected to degrade when thrust levels increased rather than improve and remain fairly constant throughout the remainder of descent and for ascent.

Pulse Torquer Servo Amplifier Intermittent Error

Several areas of electronics were identified which could cause the anomaly observed in X channel and not affect the Y and Z channels. All the areas of interest are associated with the X Gyro Pulse Torquing Servo Amplifier.

Large scale factor shifts are possible if the scale factor trim resistor shown in Figure 3-17 is intermittently opening or shortening. The scale factor change could cause uncompensated drift to occur due to the rate environment and in addition a constant bias drift would occur due to unbalanced loop gain. The shorted and open conditions were analyzed and the resultant response to body rate inputs and the residual bias drift was predicted. Comparing these predictions to the flight data showed numerous inconsistencies thus refuting a hypothesized intermittent shortening or intermittent open. A combined open-short failure mechanism is highly improbable.

If the gyro anomaly is considered "g" induced instead of "g" sensitive, the observed drift rates are expressed in deg/hr, not deg/hr/g and the magnitude of drifts shown on the bottom of Figure 3-15 can all be modified by a factor equivalent to g levels present during the periods under study. The result is; observed drift bias levels ranging from 20 deg/hr down to approximately 1 deg/hr. Two portions of the PTSA were studied which could cause the observed drift levels in one loop and not

the others. One is the bridge/driver circuit and the other is the current regulator shown in Figure 3-17. The bridge/driver has three suspect areas, the bias trim resistor, the bridge resistors or the bridge transistors. To get the maximum drift observed, a bias trim change of 1/2 ohm must occur, or one of the four bridge resistors must change 1/2 ohm, or the bridge transistor base-emitter or collector-emitter voltage must change by 0.1 volt. Different changes would be required for all other drift values observed from the gyro.

A faulty current regulator can cause drastic shifts in scale factor and with the current regulator in the full-on state, bias drifts of 40 deg/hr are possible. A failed component within the regulator could cause intermittent operation sensitive to the dynamic environment. If the intermittent condition is excited by vibratory rates, it will cause rectification of the rates resulting in apparent bias shifts.

In conclusion, it is evident that a problem in the X gyro loop caused the anomalous behavior observed on Apollo 16, and numerous failure mechanisms have been hypothesized. However, no one hypothesis fits all the flight data and the ASA test history. Combined hypotheses result in improbable considerations. Meticulous review of the preflight data for this gyro yields no suspicious areas and provides no correlation to previously known gyro failure modes. Based on the flight data available, insufficient evidence exists to attribute the anomaly to either the gyro itself or the associated electronics.

### 3.2.3 AGS-PGNCS Velocity Comparisons During Powered Flight

AGS minus PGNCS velocity comparisons in body space provide the information for assessing AGS accelerometer errors. PGNCS sensed velocity in body coordinates is obtained by rotating IMU sensed $\Delta V$ using gimbal angles and summing. AGS sensed velocity is obtained by extracting gravity from velocity state vectors and rotating the inertial velocity components into body coordinates using the Direction Cosine (DC) matrix. In theory, these differences represent only accelerometer errors since the gimbal angles are true representation of IMU to S/C space and the DC matrix is the instrument used onboard for rotating the body sensed acceleration to inertial space. The resulting

comparisons are sensed acceleration against sensed acceleration and reflect only accelerometer errors and timing errors.

### 3.2.3.1 Descent Velocity Comparisons

Start of PDI was 104:17:25.3 AET with lunar touchdown occurring at 104:29:36 AET. Total accumulated velocity during the descent phase was approximately 6720 fps. Figures 3-19 through 3-21 show the velocity differences obtained for descent after correction for known PGNCS bias errors. The step changes reflected in the X channel are the result of postflight data processing error and should be ignored. Using a weighted least squares filter with the AGS accelerometer error model, a set of error coefficients was determined which fit the velocity difference curves. Modeled accelerometer errors are listed in Table 3.4. The fit was terminated at the P64 point so as not to corrupt the fit with the poor quality telemetry data which existed until touchdown. Results of the fit are listed below:

| Error Model Symbol | Description | Value |
|---|---|---|
| XAB | X accelerometer static bias | -22 μg |
| YAB | Y accelerometer static bias | -39 μg |
| ZAB | Z accelerometer static bias | -16 μg |
| YAMTX | Y accelerometer misalignment toward X | -98 arc sec |
| ZAMTX | Z accelerometer misalignment toward X | 72 arc sec |
| TB | Accelerometer timing bias | -0.13 sec |

The accelerometer bias errors were constrained in the fit to agree with static bias values determined before PDI ignition and are recoverable from Table 3.1 as the difference between Columns (4) and (2). In the X

channel, all of the observed velocity error was accountable to static bias thus indicating the absence of dynamic error and scale factor error. For the Y channel, all of the dynamic error has been solved for in terms of Y accelerometer misalignment toward X (YAMTX) because the only other significant error source, dynamic accelerometer error is highly correlated with misalignment and inseparable. For the Z channel, misalignment and dynamic bias are similarly inseparable.

3.2.3.2 Ascent Velocity Comparisons

Liftoff from the lunar surface was at 175:31:47.8 AET with insertion occurring at 175:38:56 AET. Total accumulated velocity during the ascent phase was approximately 5802 fps. Ascent velocity differences were developed in the same manner described in Section 3.2.3.1, and are presented in Figures 3-22 through 3-24. PGNCS known bias errors have been removed from these differences. No strong recognizable error sources are distinquishable from the observed differences and it appears that X and Z accelerometer errors are lost in the noise level of telemetry data obtained (approximately 0.5 fps). The observed stair case pattern in the Z channel is not representative of system error but is the result of postflight data interpolation in an attempt to duplicate lost data during telemetry dropout periods. However, for both Y and Z channels some slight trending is evident in the data and the slope can be fit with accelerometer misalignment toward X of the same sign observed during descent. For ascent all of the estimated accelerometer errors are listed below:

| Error Model Symbol | Description | Value |
|---|---|---|
| XAB | X accelerometer static bias | -31 μg |
| YAB | Y accelerometer static bias | -35 μg |
| ZAB | Z accelerometer static bias | -20 μg |
| YAMTX | Y accelerometer misalignment toward X | -36 arc sec |
| ZAMTX | Z Accelerometer misalignment toward X | 22 arc sec |

The accelerometer static biases were based on a segment of free-fall data after completion of orbit insertion and are traceable to the difference between Column (5) and (2) in Table 3.1.

### 3.2.4 Comparisons of ASA Inflight Errors

#### 3.2.4.1 Accelerometer Error Summary

Based on preflight calibration data for ASA 013, the system flown on Apollo 16, the accelerometer inflight performance was in close agreement with the preflight estimate error model.

For powered flight, accelerometer errors are summarized in Table 3.5. As noted in Section 3.2.3, individual accelerometer dynamic error terms are not fully separable and as a result, the observed dynamic error was arbitrarily grouped into one error source for each axis. To perform comparisons of inflight data to preflight estimates, again it was necessary to define a single performance index which could represent the premission performance estimates and the inflight estimate. The chosen performance index was micro gravities and all sensing axes misalignments were converted to equivalent acceleration error. This is possible only because the ratios of the partials for the bias error and misalignment errors are fairly constant throughout the descent and ascent trajectories thus explaining the high correlation between these errors.

Table 3.5 shows reasonable corroboration of errors with the preflight system modeling for ASA 013 and good agreement between the inflight values for the two phases of flight.

#### 3.2.4.2 Gyro Error Summary

Due to the questionable nature of the X gyro loop observed performance, comparisons of the X gyro inflight data with preflight estimates is somewhat arbitrary. But for completeness, the X gyro data has been included in the gyro bias summary Table 3.6. The inflight estimate for the X gyro drift in powered flight indicates the range of measured data from the integrated body rate difference plots after compensation for the assumed fixed drift error. The fixed drift values shown in Table 3.6 for descent are the

measured AGS divergence from PGNCS before PDI. The fixed drift values for ascent are the AGS residual drifts after orbit insertion corrected for the compensation error. The Y and Z gyros show reasonable corroboration of the preflight error model and good agreement between flight phases.

Table 3.1. ASA 013 Accelerometer Static Bias History (ug)

| Acceleration | (1) Preflight Calibration Mean | (2) Inflight Calibration | (3) Nominal PDI Pass Rev 13 | (4) Actual PDI Pass Rev 16 | (5) Post Ascent |
|---|---|---|---|---|---|
| X | 280 | 249 | 221 | 224 | 218 |
| Y | - 31 | - 31 | - 68 | - 71 | - 66 |
| Z | - 62 | - 62 | - 84 | - 78 | - 82 |

Table 3.2. ASA 013 Gyro Static Drift History (Deg/Hr)

| Gyro | (1) Preflight Calibration Mean | (2) Inflight Calibration | (3) Pre-Descent | (4) Prelift Lunar Surface Calibration | (5) Post Ascent |
|---|---|---|---|---|---|
| X | 0.03 | -0.06 | 0.01 | 1.13* | -0.45 to 0.77 |
| Y | -0.29 | -0.45 | -0.51 | -0.60 | -0.60 |
| Z | 0.55 | 0.29 | 0.13 | 0.64 | 0.64 |

*Includes some spin axis mass unbalance gyro drift.

Table 3.3 X Gyro Spin Axis Mass Unbalance Instability Failure Mechanisms

| | Gyro Component | Part Failure | Sufficient Torque to cause the Observed Drift? | Could the Gyro Recover? |
|---|---|---|---|---|
| INNER FLOAT | 1. Bearing | Inner race movement of 0.05 in. | yes | no |
| | | Outer race movement of 0.03 in. | yes | no |
| | | Ball track change due to pre-load yield | no | N/A |
| | | Retainer changes position | no | N/A |
| | | Retainer oil leak | no | N/A |
| | 2. Stator Assembly | Shaft movement | yes | yes |
| | | Stop nut unscrews | no | N/A |
| | 3. Spin Motor | Spin wheel picks up or looses mass | yes | no |
| | | Dowel pins move out | yes | no |
| | | Clamping screws shift position | yes | no |
| | | SMRD magnets shift position | no | N/A |
| | | Hysteresis ring position shift | no | N/A |
| | 4. Float | Particle in the inner float | no | N/A |
| | | Damping fluid leaking into inner float | yes | yes |
| FLOAT ASSEMBLY | 1. Float Halves | Float halves change shape | no | N/A |
| | | Float assembly gains or loses mass | no | N/A |
| | | Float halves lose epoxy seal | no | N/A |
| | 2. Balance Weights | Weights shift position | no | N/A |
| | | Weights break or separate | yes | no |
| | | Weights absorb fluid | yes | no |
| | 3. Torquer Pick-off Assembly | Assembly shifts position | yes | no |
| | | Assembly absorbs fluid in potting | no | N/A |

Table 3.3 X Gyro Spin Axis Mass Unbalance Instability
Failure Mechanisms (Continued)

| | Gyro Component | Part Failure | Sufficient Torque to cause the Observed Drift? | Could the Gyro Recover? |
|---|---|---|---|---|
| OUTER FLOAT | 1. Flex leads | Leads move | no | N/A |
| | | Leads change mass | no | N/A |
| | | Flex lead clips move | no | N/A |
| | | Flex lead conductive epoxy absorbs fluid | no | N/A |
| | | Flex leads change shape | no | N/A |
| | 2. Float | Foreign particle on float | no | N/A |
| | | Bubble attached to float | no | N/A |
| | | Foreign particle between float and case | yes | yes |
| | | Bubble between float and case | yes | yes |
| | 3. Damping fluid | Stratification or solidification of fluid | yes | no |
| | 4. Pivot and jewels | Broken pivot | Yes | Highly improbable |
| | | Cracked jewel | yes | no |
| | | Broken endstone | yes | Highly improbable |
| | 5. Balance forks | Fork moves and touches balance screw "T" bar | no | N/A |
| | 6. Torquer magnet assembly | Magnet moves out | yes | no |

Table 3.4. LM AGS Error Model (Accelerometer)

| Mnemonic | Description |
|---|---|
| XAB | X accelerometer bias |
| YAB | Y accelerometer bias |
| ZAB | Z accelerometer bias |
| XASF | X accelerometer scale factor |
| XAMTY | X accelerometer misalignment toward Y |
| XAMTZ | X accelerometer misalignment toward Z |
| YAMTX | Y accelerometer misalignment toward X |
| YASF | Y accelerometer scale factor |
| YAMTZ | Y accelerometer misalignment toward Z |
| ZAMTX | Z accelerometer misalignment toward X |
| ZAMTY | Z accelerometer misalignment toward Y |
| ZASF | Z accelerometer scale factor |
| TB | Accelerometer timing bias |

Table 3.5 Accelerometer Error Summary

Descent Equivalent Accelerometer Bias Errors (ug)

| Axis | Error Source | Inflight Estimate | ASA 013 Preflight Estimate Mean | ASA 013 Preflight Estimate 3σ |
|---|---|---|---|---|
| X | Bias, nonlinearity and dynamic errors | | -21 | 101 |
| | Scale factor | | 14 | 63 |
| | TOTAL | -22 | - 7 | 119 |
| Y | Bias, nonlinearity and dynamic errors | | -12 | 88 |
| | Internal sensing axis alignment | | -89 | 33 |
| | ASA alignment to navigation base | | 0 | 178 |
| | TOTAL | -179 | -101 | 201 |
| Z | Bias, nonlinearity and dynamic errors | | - 6 | 88 |
| | Internal sensing axis alignment | | 69 | 11 |
| | ASA alignment to navigation base | | 0 | 178 |
| | TOTAL | 87 | 63 | 199 |

Ascent Equivalent Accelerometer Bias Errors (ug)

| Axis | Error Source | Inflight Estimate | ASA 013 Preflight Estimate Mean | ASA 013 Preflight Estimate 3σ |
|---|---|---|---|---|
| X | Bias, nonlinearity and dynamic errors | | -21 | 113 |
| | Scale factor | -31 | 19 | 99 |
| | TOTAL | | - 2 | 150 |
| Y | Bias, nonlinearity and dynamic errors | | -12 | 101 |
| | Internal sensing axis alignment | | -134 | 49 |
| | ASA alignment to navigation base | | 0 | 265 |
| | TOTAL | -112 | -146 | 288 |
| Z | Bias, nonlinearity and dynamic errors | | - 6 | 95 |
| | Internal sensing axis alignment | | 103 | 17 |
| | ASA alignment to navigation base | | 0 | 265 |
| | TOTAL | 27 | 97 | 282 |

Table 3.6 Gyro Bias Error Summary (Deg/Hr)

| | Descent | | | |
|---|---|---|---|---|
| | ASA 013 Preflight Estimate | | | ASA 013 Inflight Estimate |
| | Mean | 3σ | | |
| X Gyro fixed drift | 0 | 0.45 | | 0.07 |
| Y Gyro fixed drift | 0 | 0.46 | | - 0.06 |
| Z Gyro fixed drift | 0 | 0.46 | | - 0.16 |
| X Gyro spin axis mass unbalance | 0 | 0.59 | (1) | 18.5 to 1.87 |
| X Gyro dynamic drift | 0.06 | 0.29 | | |
| Y Gyro dynamic drift | -0.17 | 0.26 | | - 0.37 |
| Z Gyro dynamic drift | -0.04 | 0.25 | | 0.08 |
| X Total drift (deg/hr) | 0.06 | 0.80 | | 19.2 to 1.94 |
| Y Total drift (deg/hr) | -0.17 | 0.53 | | - 0.36 |
| Z Total drift (deg/hr) | -0.04 | 0.52 | | - 0.08 |

| | Ascent | | | |
|---|---|---|---|---|
| | ASA 013 Preflight Estimate | | | ASA 013 Inflight Estimate |
| | Mean | 3σ | | |
| X Gyro fixed drift | 0 | 0.45 | | -0.45 to 0.77 |
| Y Gyro fixed drift | 0 | 0.46 | | 0 |
| Z Gyro fixed drift | 0 | 0.46 | | 0 |
| X Gyro spin axis mass unbalance | 0 | 0.59 | (1) | 4.83 to 3.61 |
| X Gyro dynamic drift | 0.06 | 0.30 | | |
| Y Gyro dynamic drift | -0.15 | 0.31 | | - 0.48 |
| Z Gyro dynamic drift | -0.03 | 0.35 | | 0 |
| X Total drift (deg/hr) | 0.06 | 0.80 | | 4.38 |
| Y Total drift (deg/hr) | -0.15 | 0.55 | | - 0.48 |
| Z Total drift (deg/hr) | -0.03 | 0.58 | | 0 |

(1) Postflight data are not sufficient to separate X gyro spin axis unbalance and gyro dynamic drift.

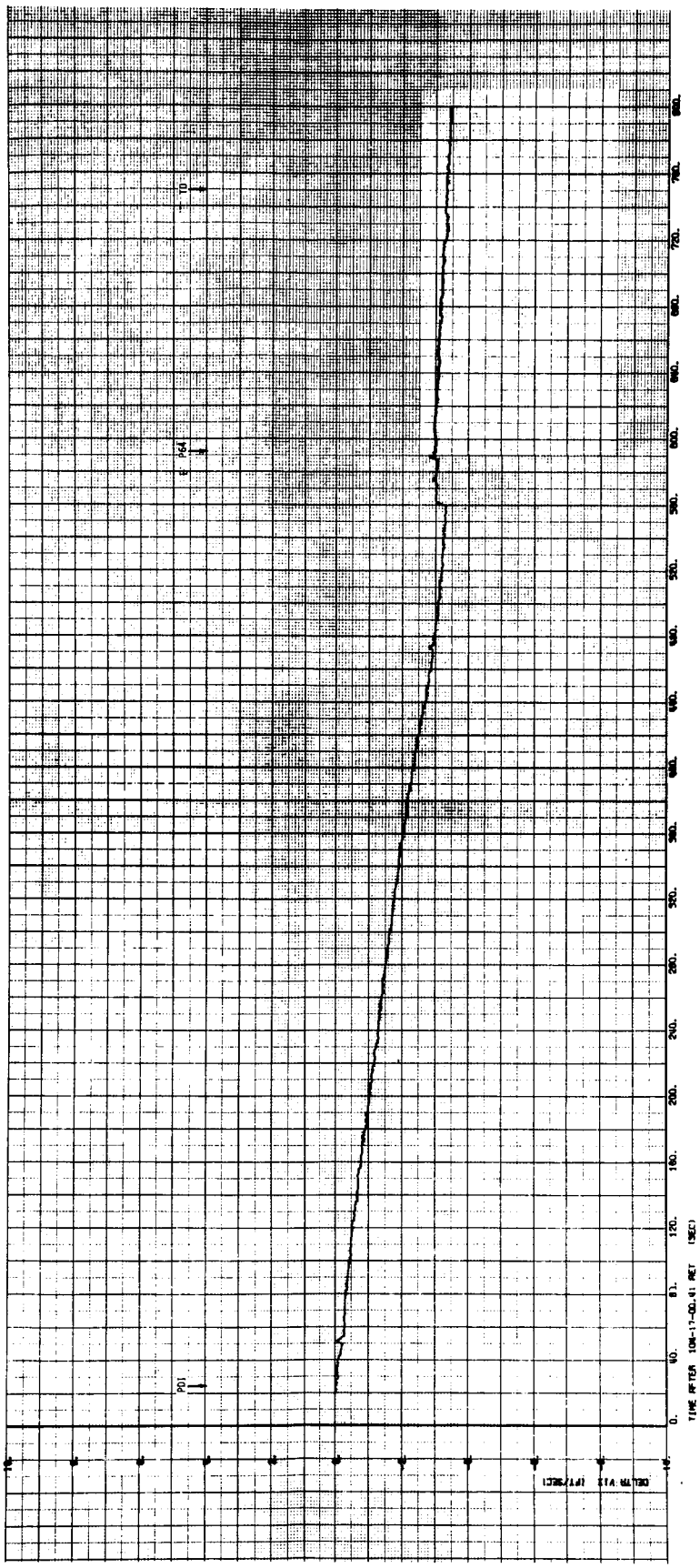


Figure 3-1. Apollo-16 LM Descent
Delta VI (PGS-AGS)

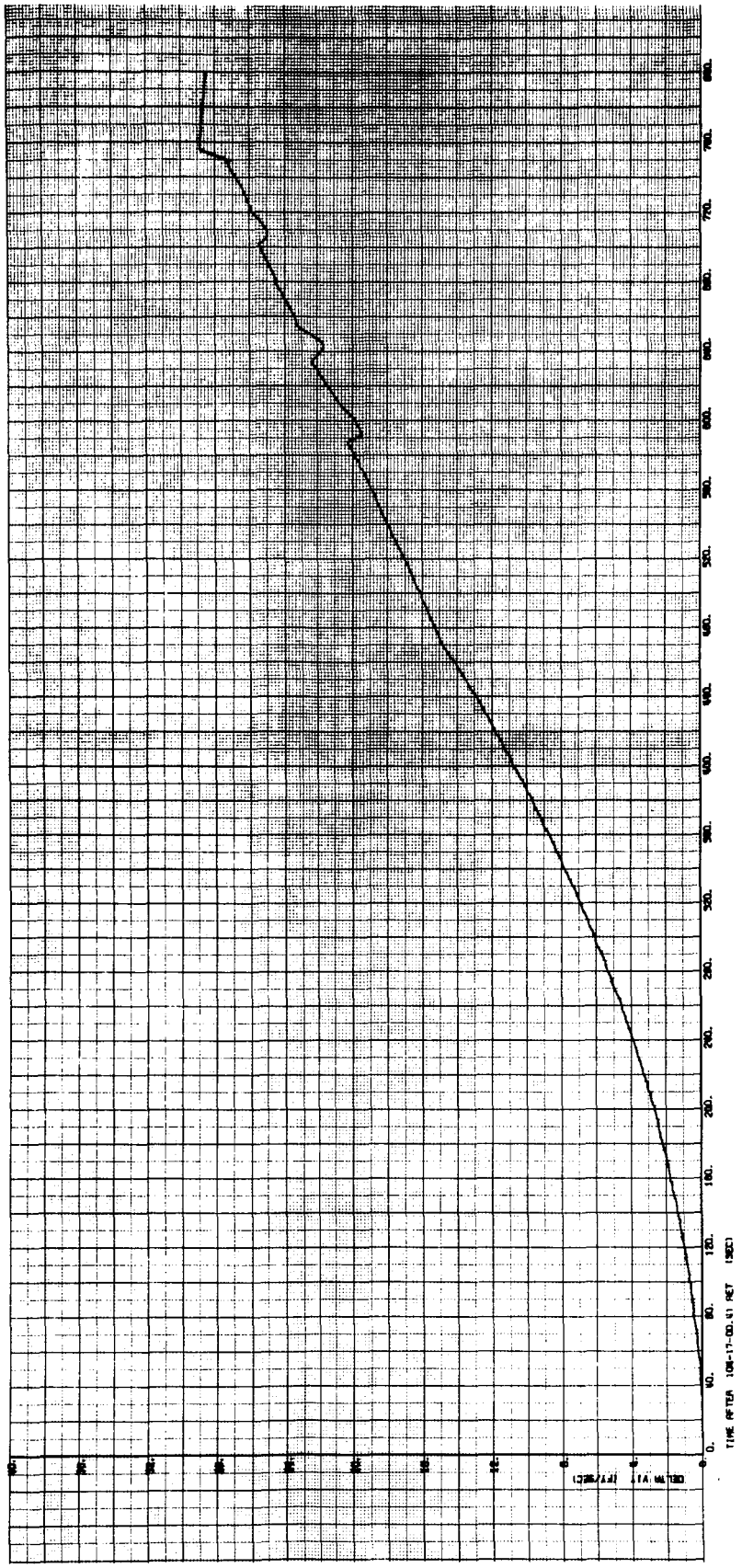


Figure 3-2. Apollo-16 LM Descent
Delta VI (PGS-AGS)

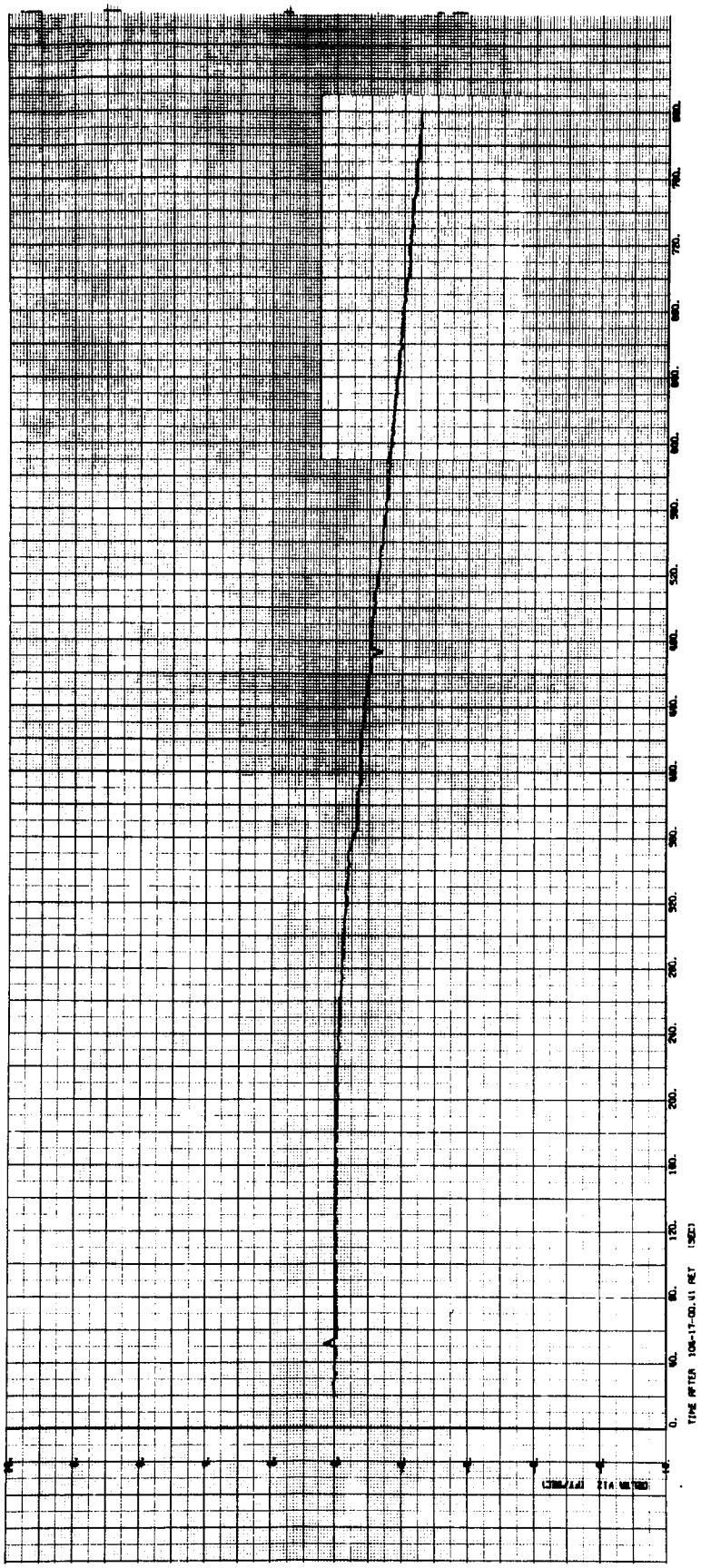

Figure 3-3. Apollo-16 LM Descent
DELTA VI (PGS-AGS)

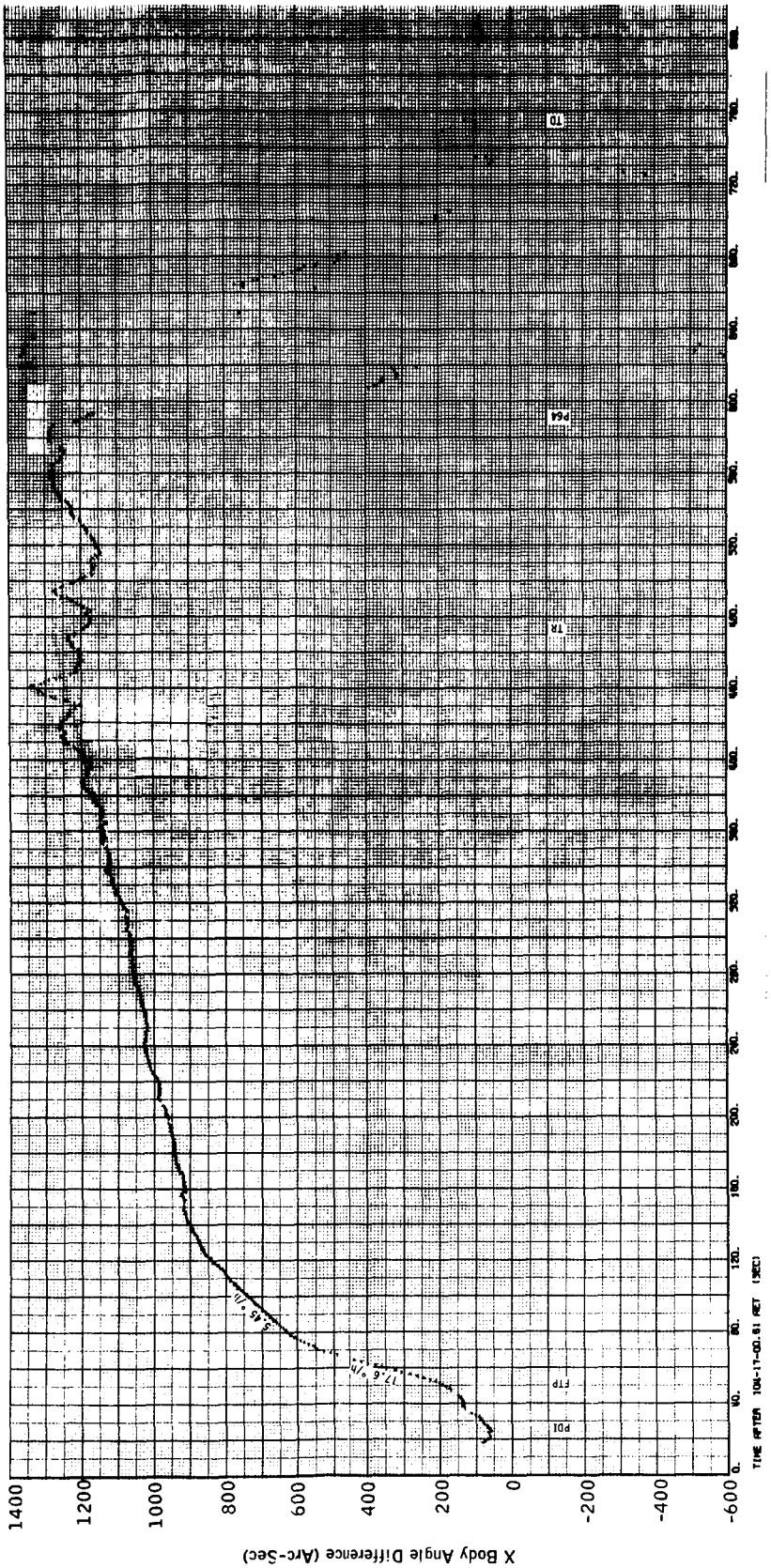


Figure 3-4. Apollo-16 LM Descent Body Angle Difference (AGS-PGS)

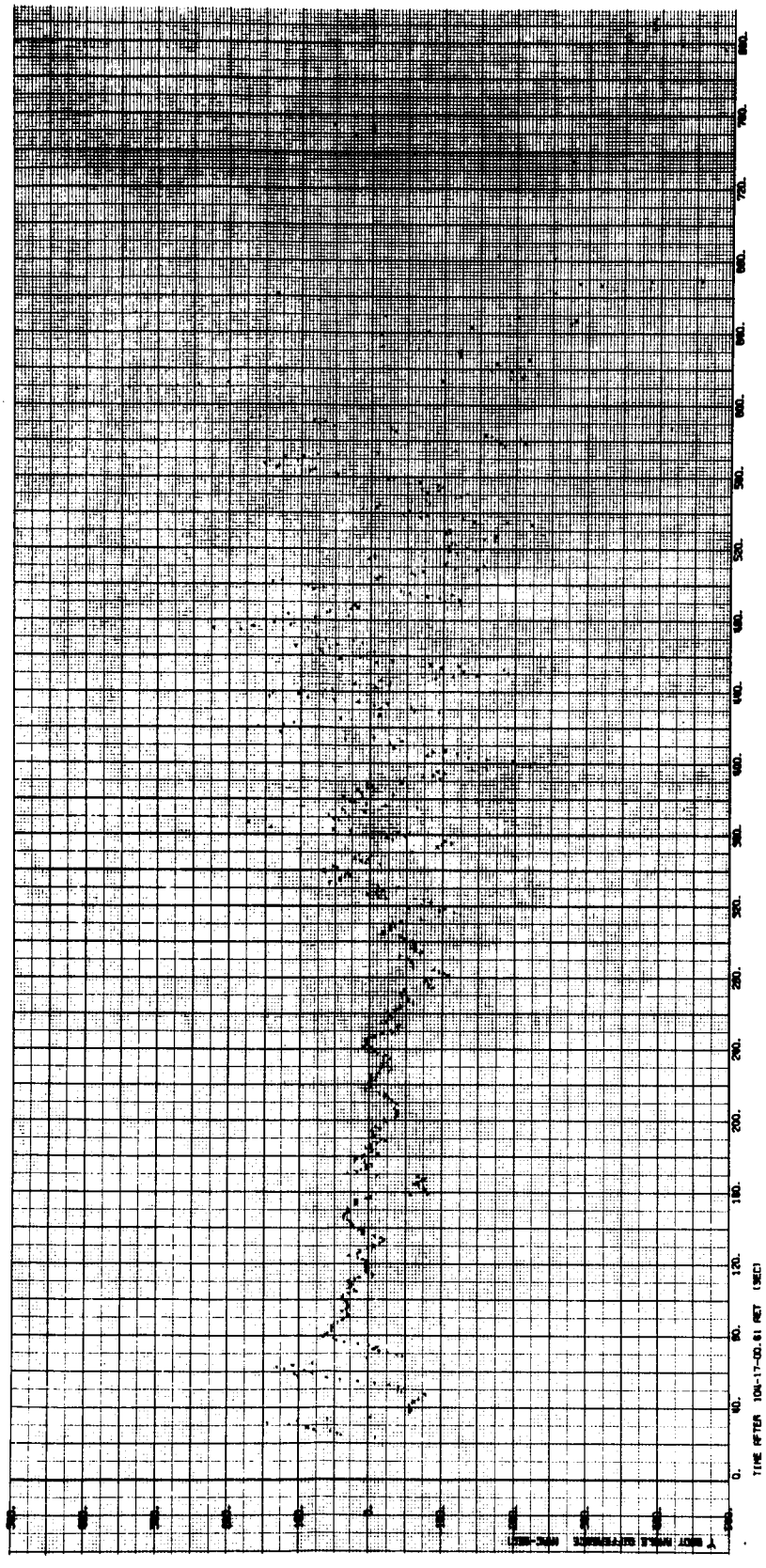


Figure 3-5. Apollo-16 LM Descent Body Angle Difference (AGS-PGS)

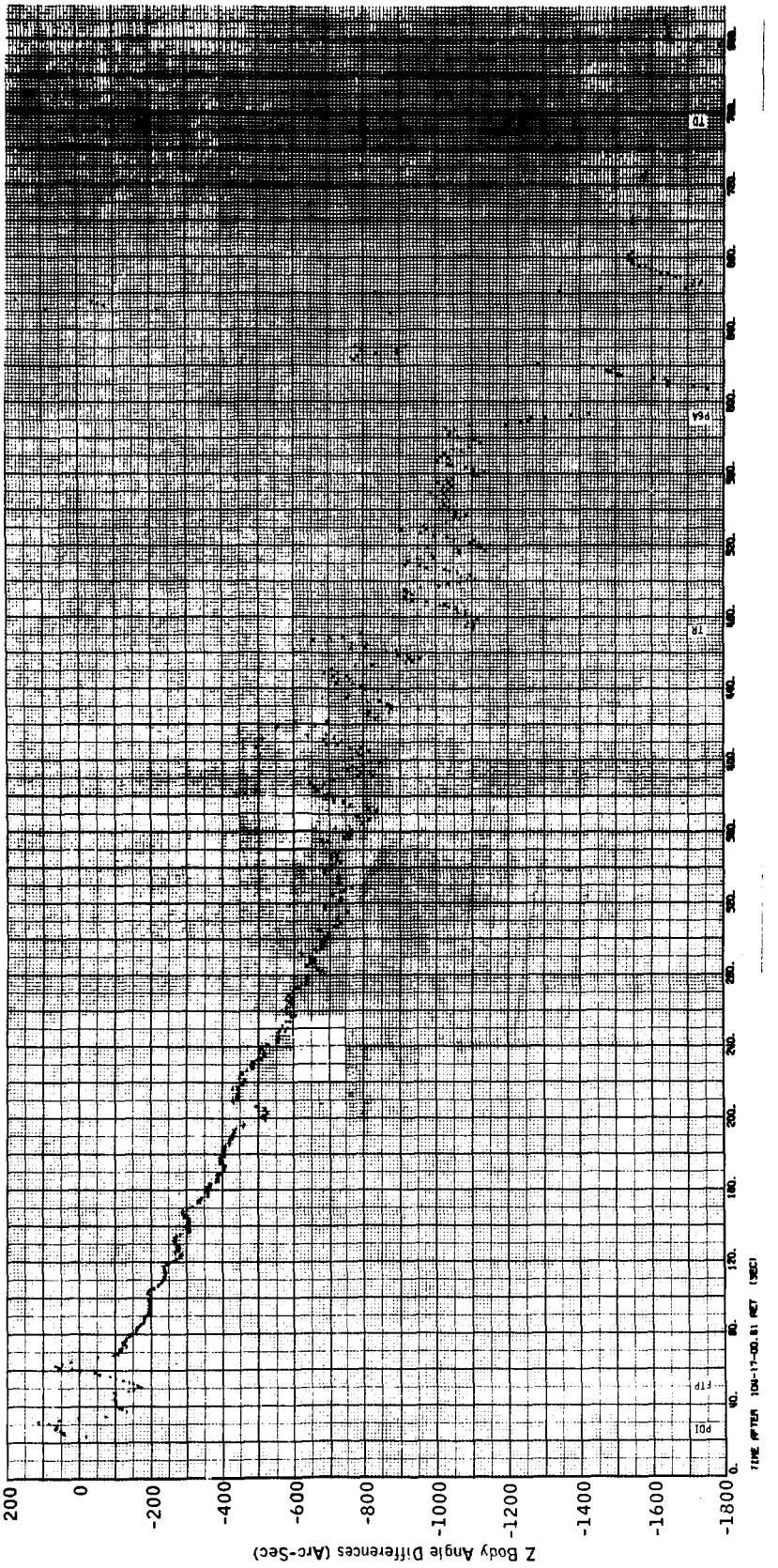


Figure 3-6. Apollo-16 LM Descent Body Angle Difference (AGS-PGS)

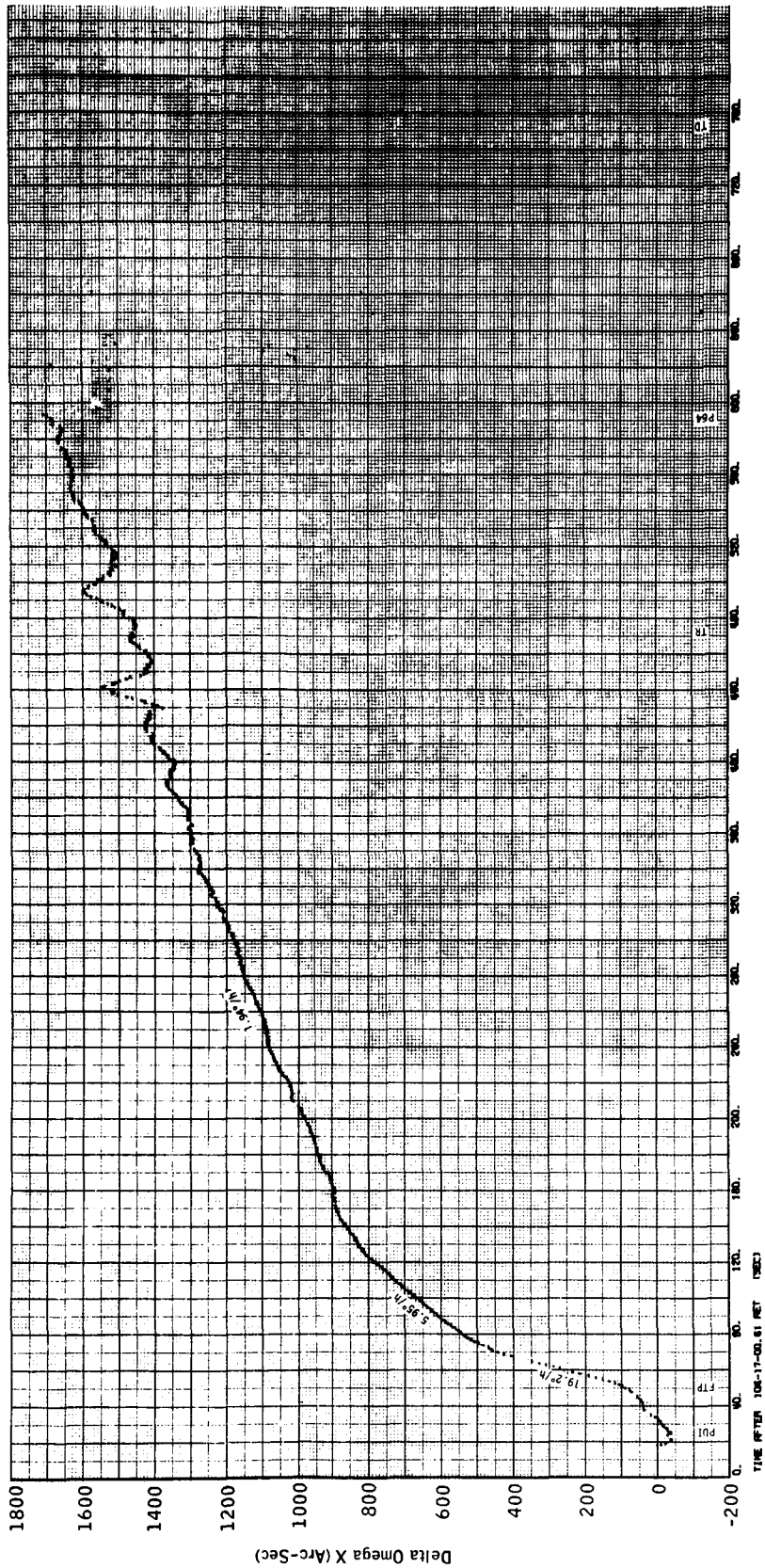


Figure 3-7. Apollo-16 LM Descent Integrated Body Rate Difference (AGS-PGS)

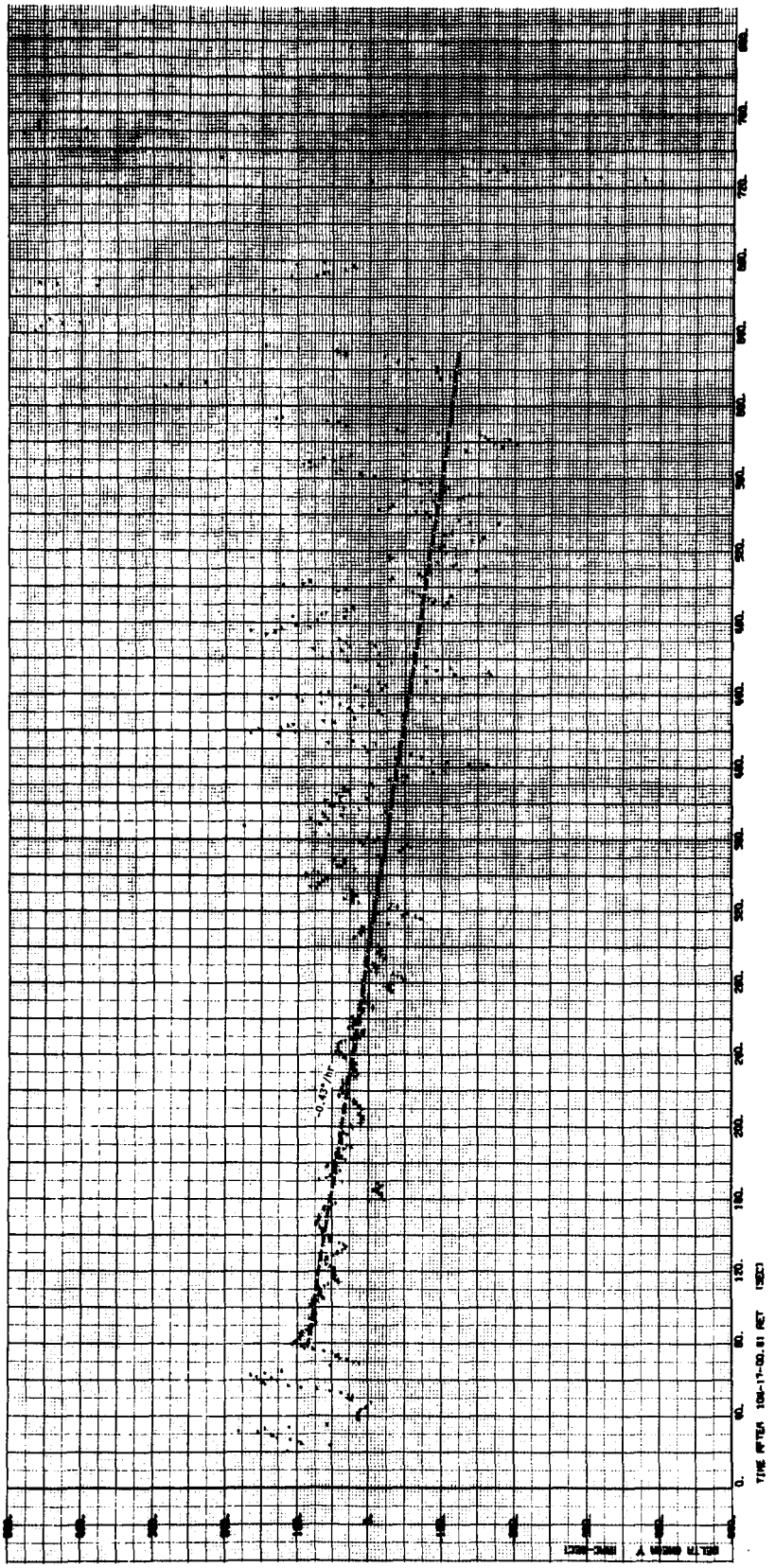


Figure 3-8. Apollo-16 LM Descent Integrated Body Rate Difference (AGS-PGS)

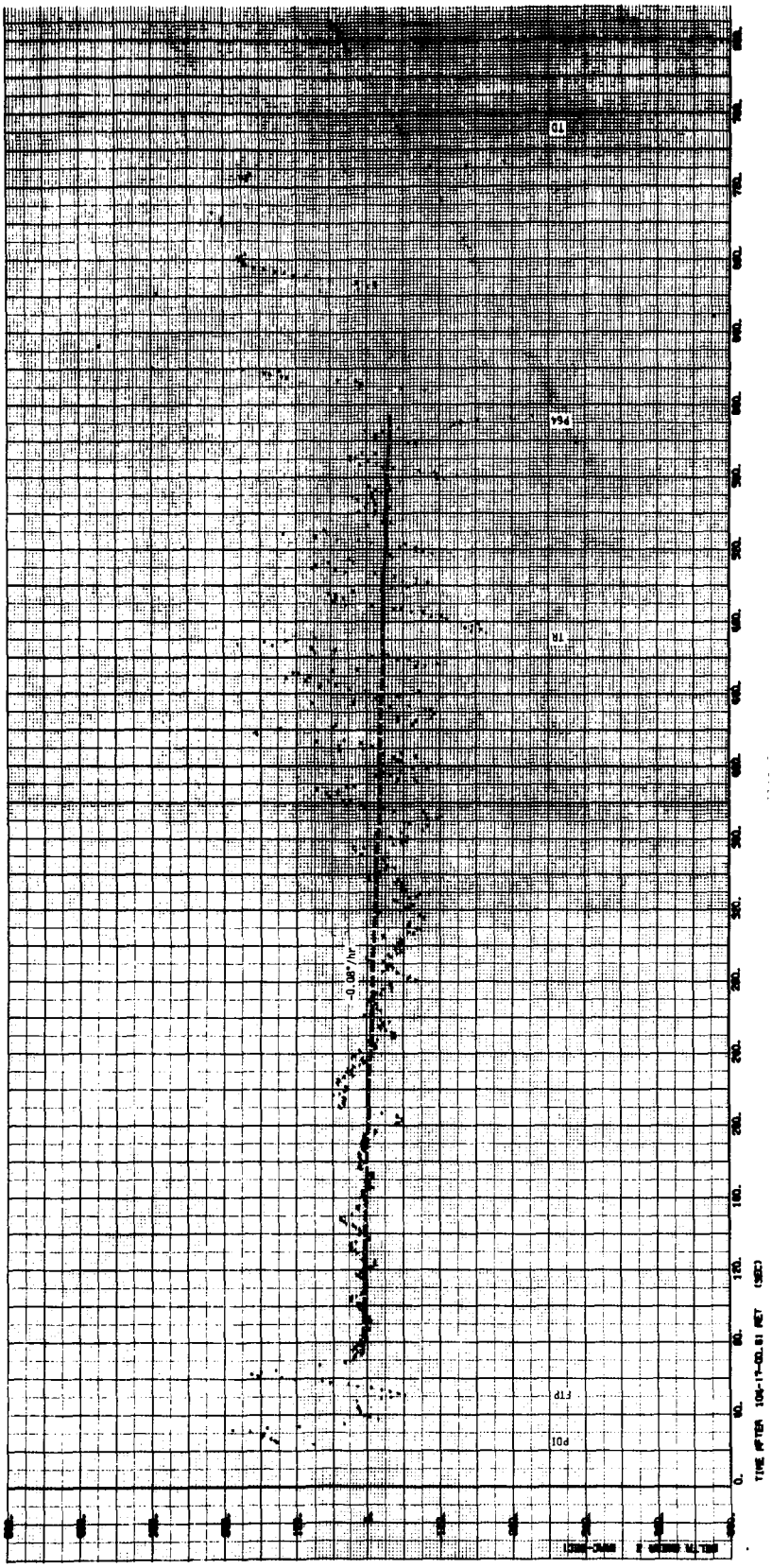


Figure 3-9. Apollo-16 LM Descent Integrated Body Rate Difference (AGS-PGS)

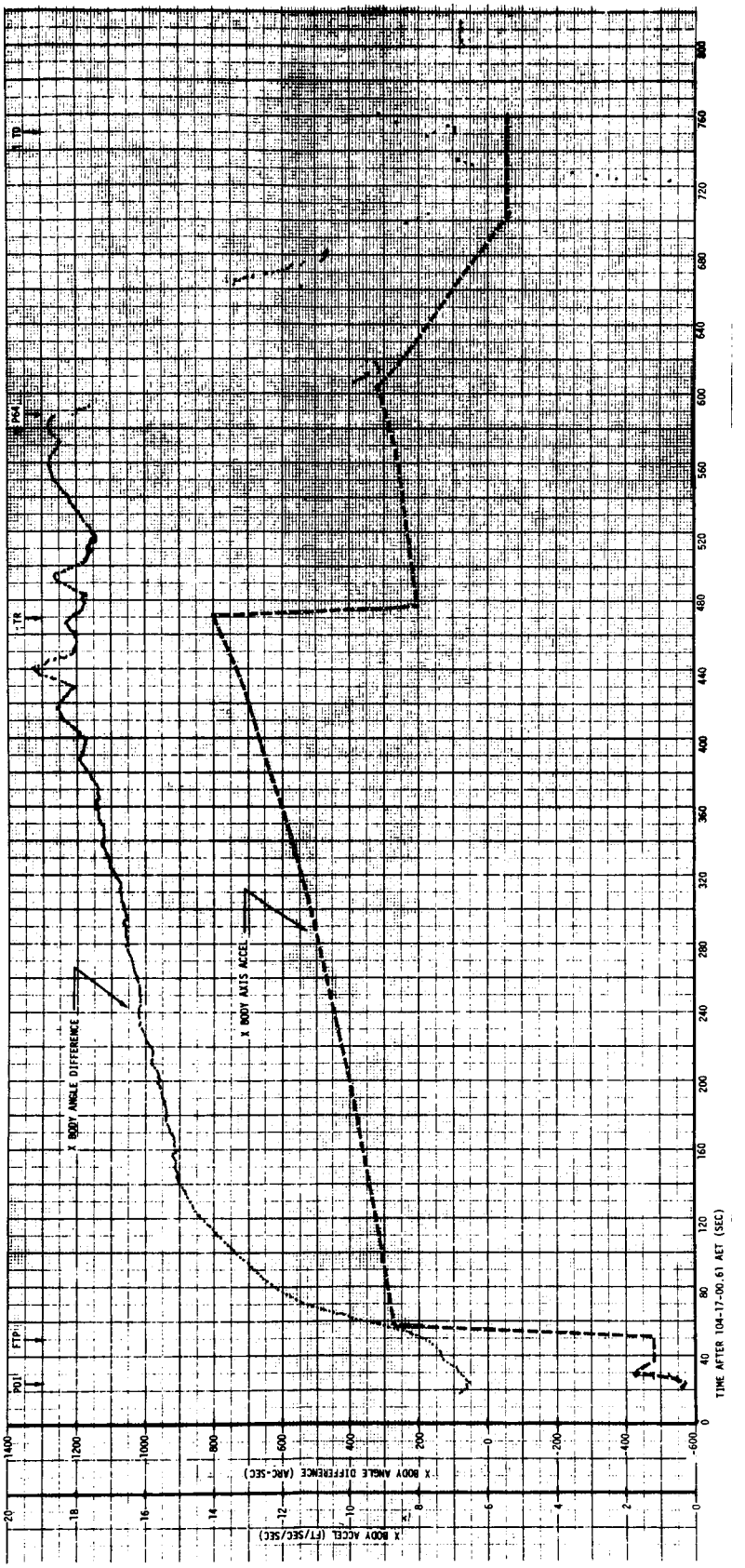


Figure 3-10. X Body Angle Difference and X Body Axis Acceleration

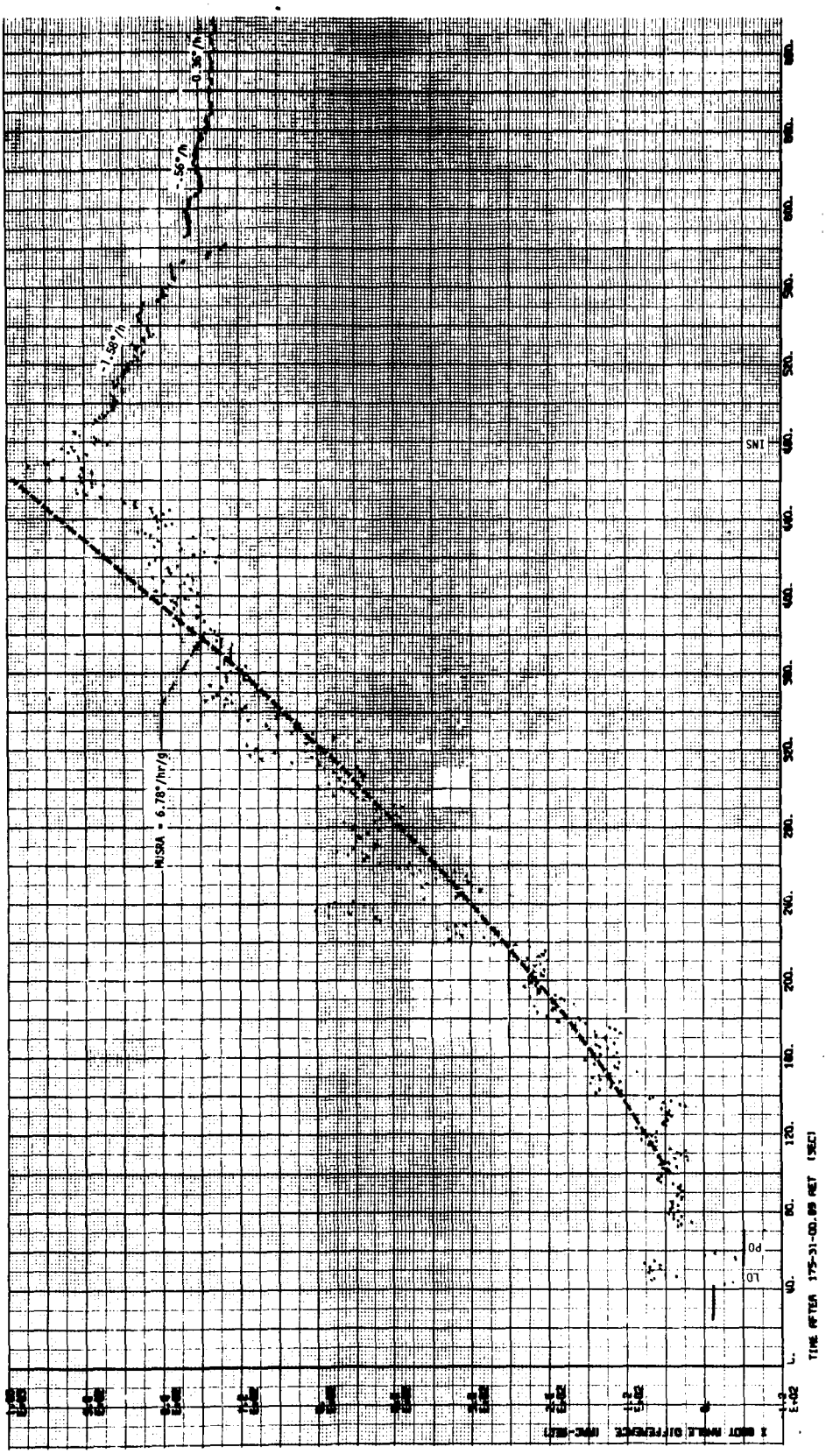


Figure 3-11. Apollo-16 LM Ascent Body Angle Difference (AGS-PGS)

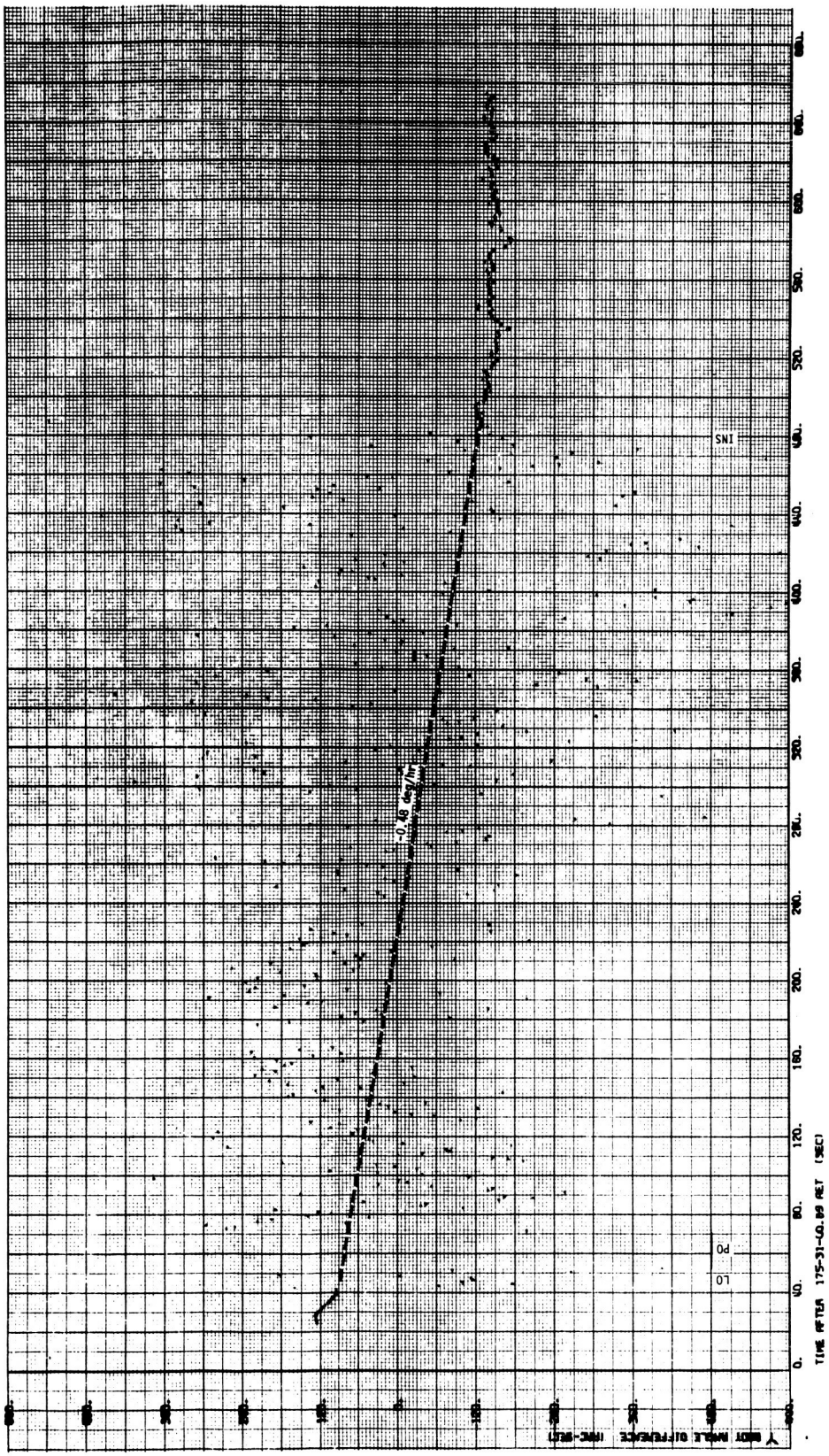


Figure 3-12. Apollo-16 LM Ascent Body Angle Difference (AGS-PGS)

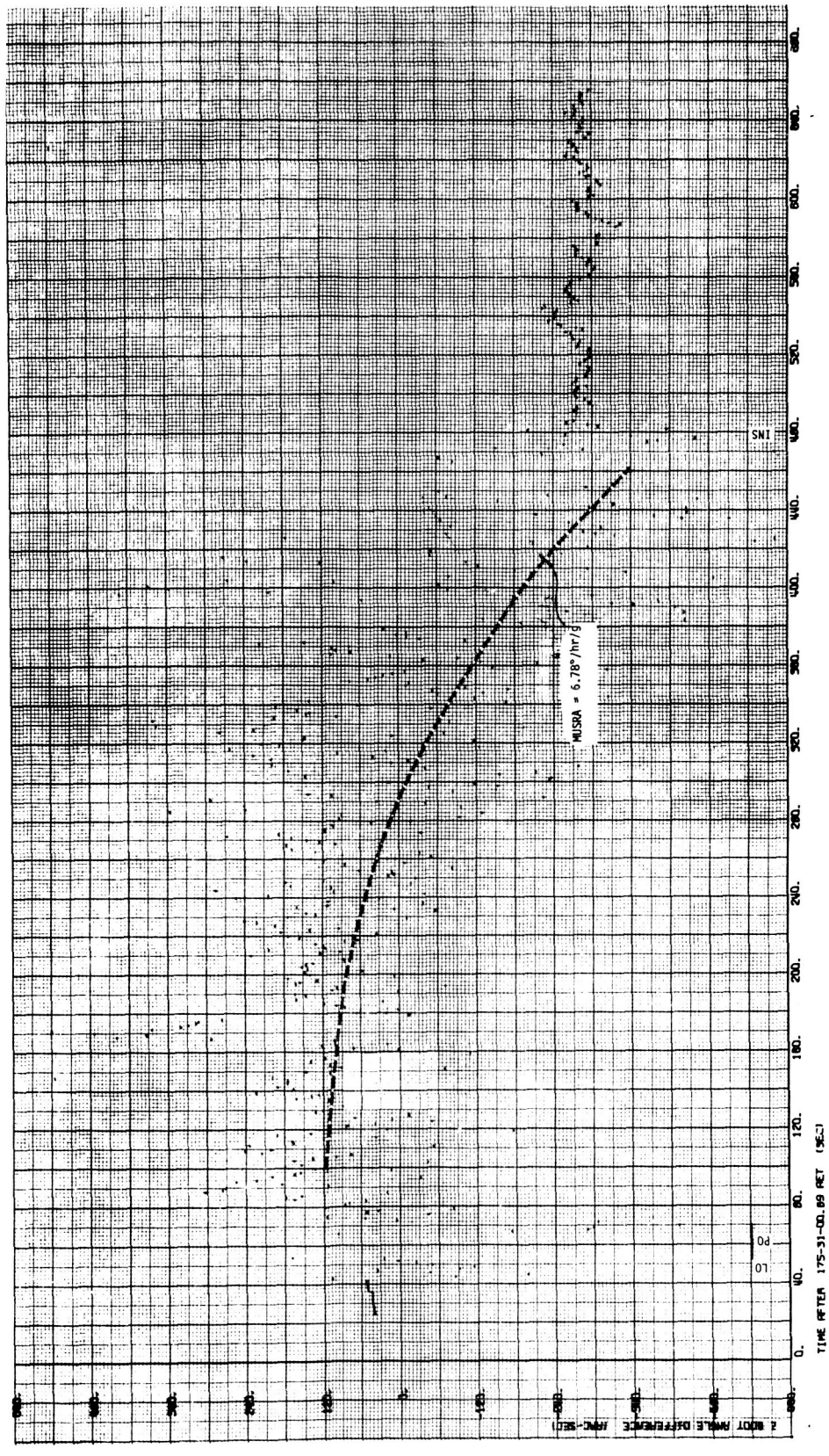


Figure 3-13. Apollo-16 LM Ascent Body Angle Difference (AGS-PGS)

Figure 3-14. Apollo 16 LM Ascent Integrated Body Rate Difference(AGS-PGS)

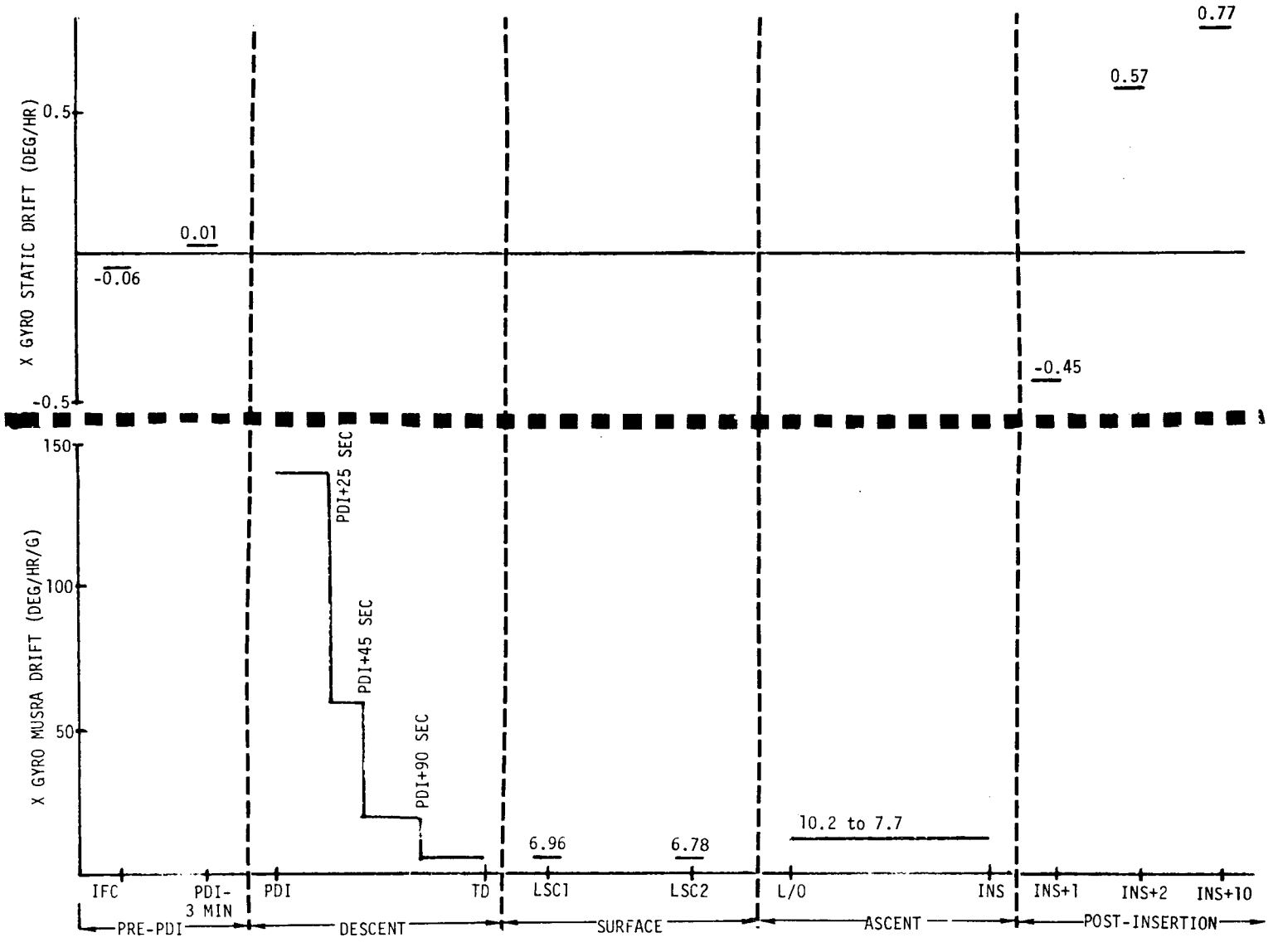


Figure 3-15. Apparent X Gyro Loop Mission Performance

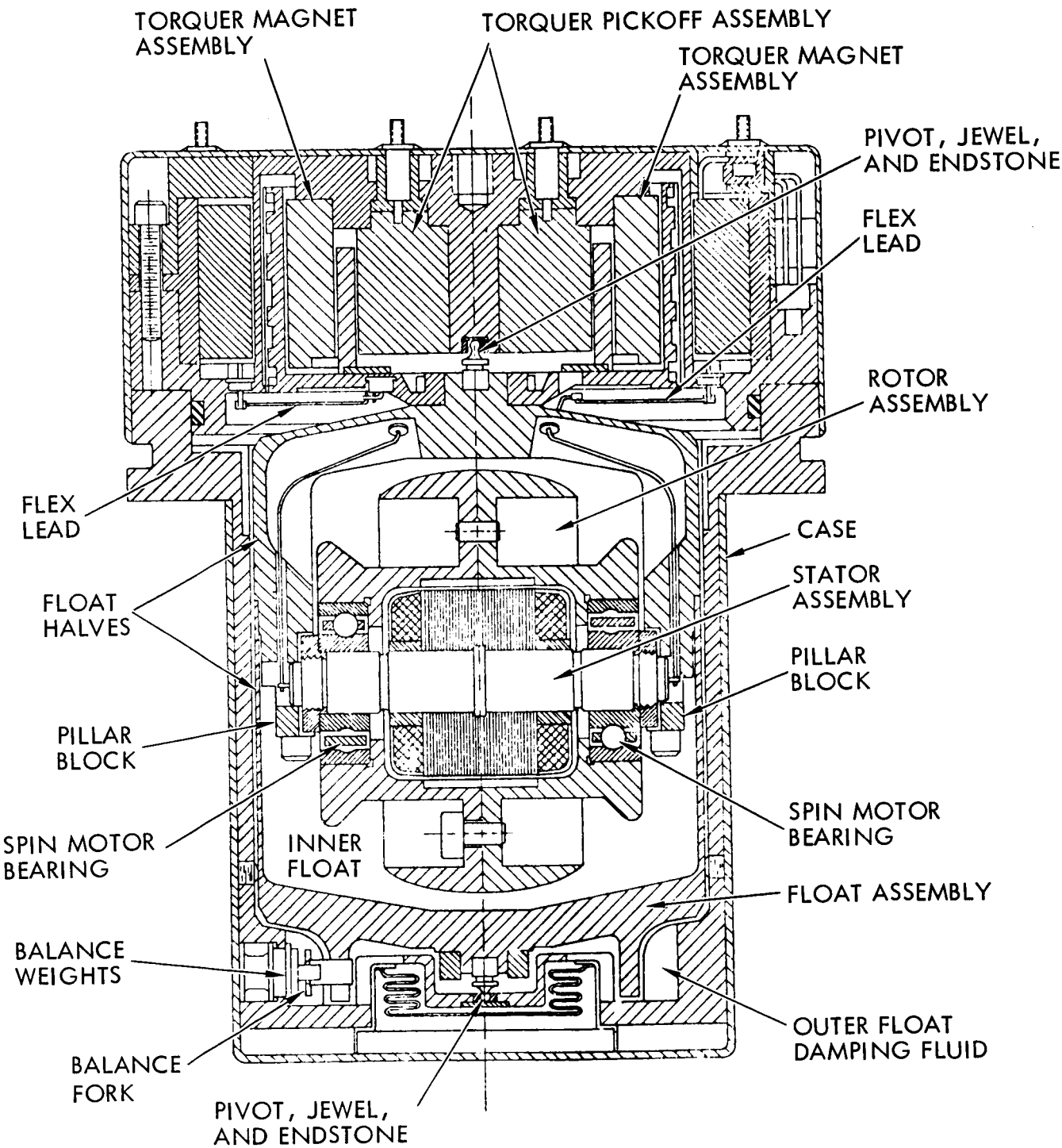


Figure 3-16. Cross Section View, Norden RI-1139 Gyroscope

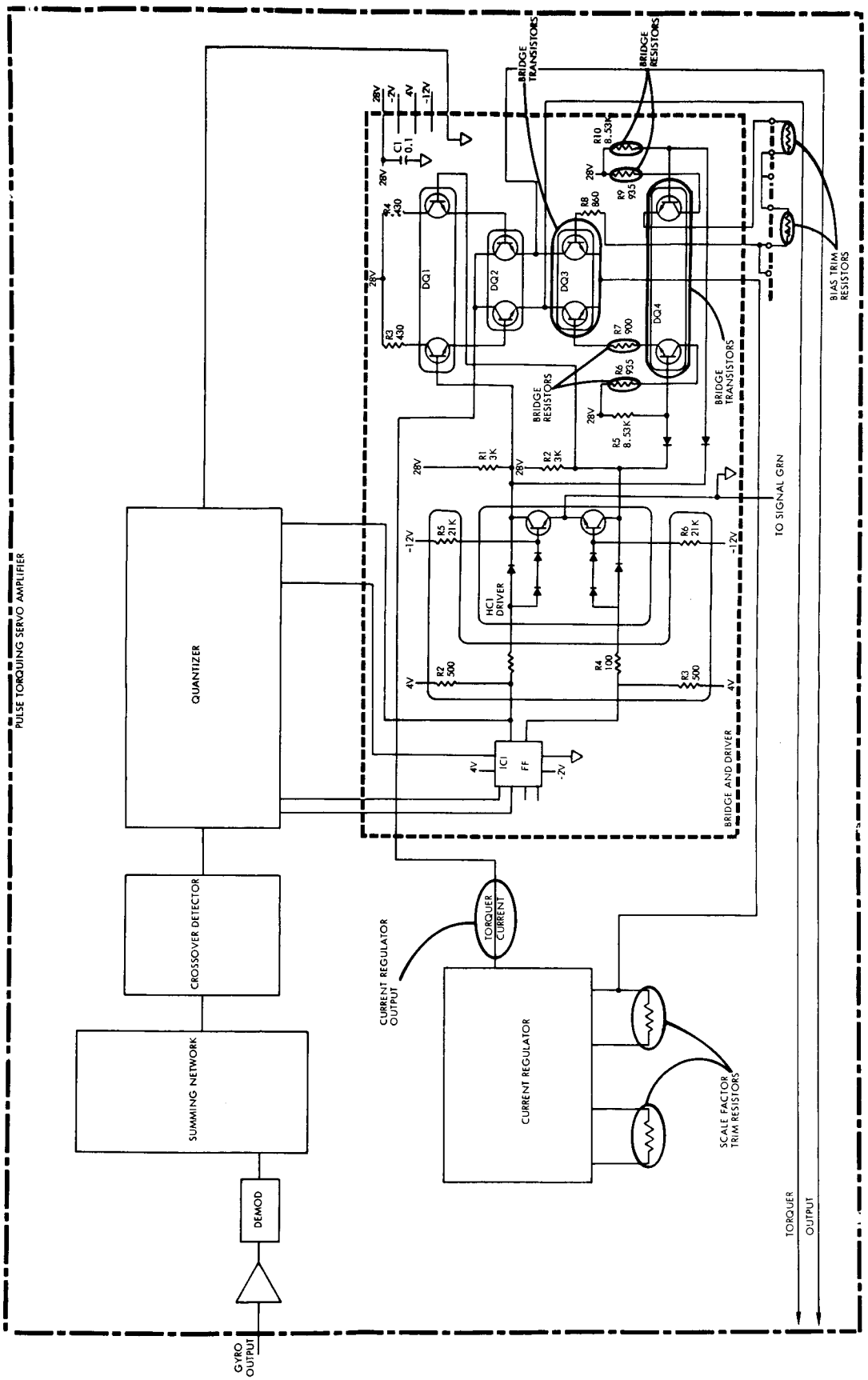


Figure 3-17. X Gyro Loop Pulse Torquing Servo Amplifier

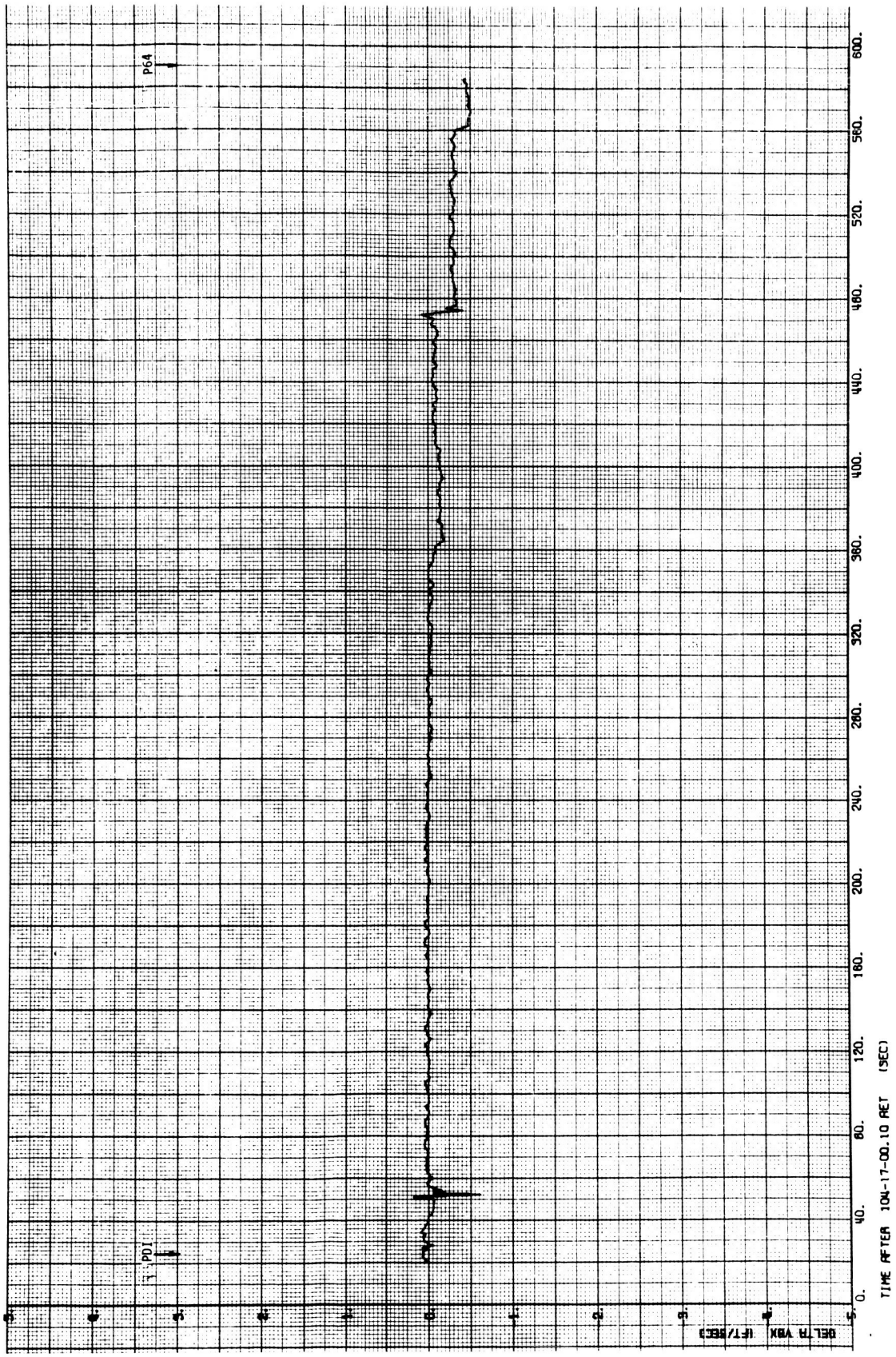


Figure 3-18. Apollo-16 LM Descent Delta VB (AGS-PGS)

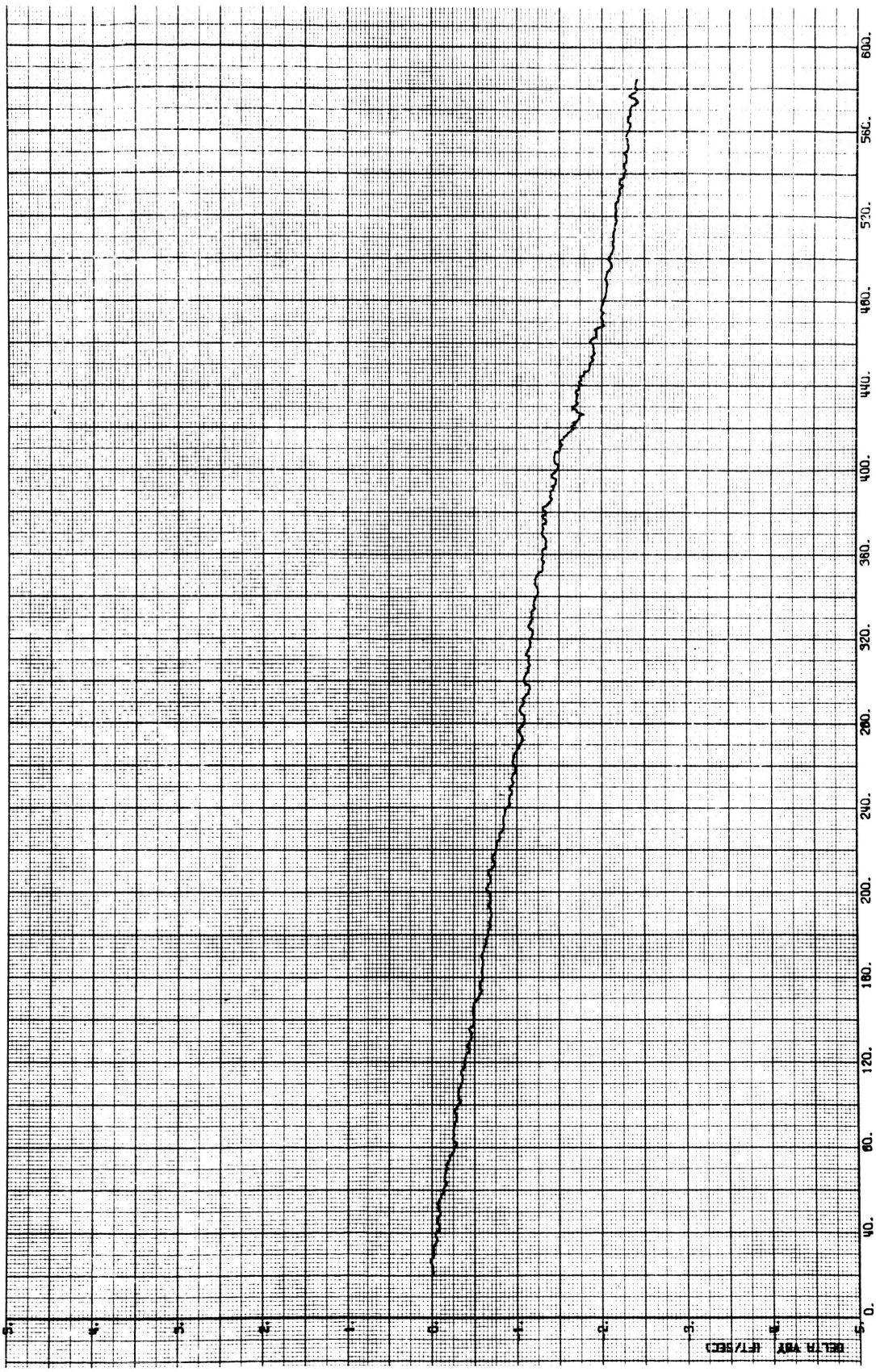


Figure 3-19. Apollo-16 LM Descent Delta VB (AGS-PGS)

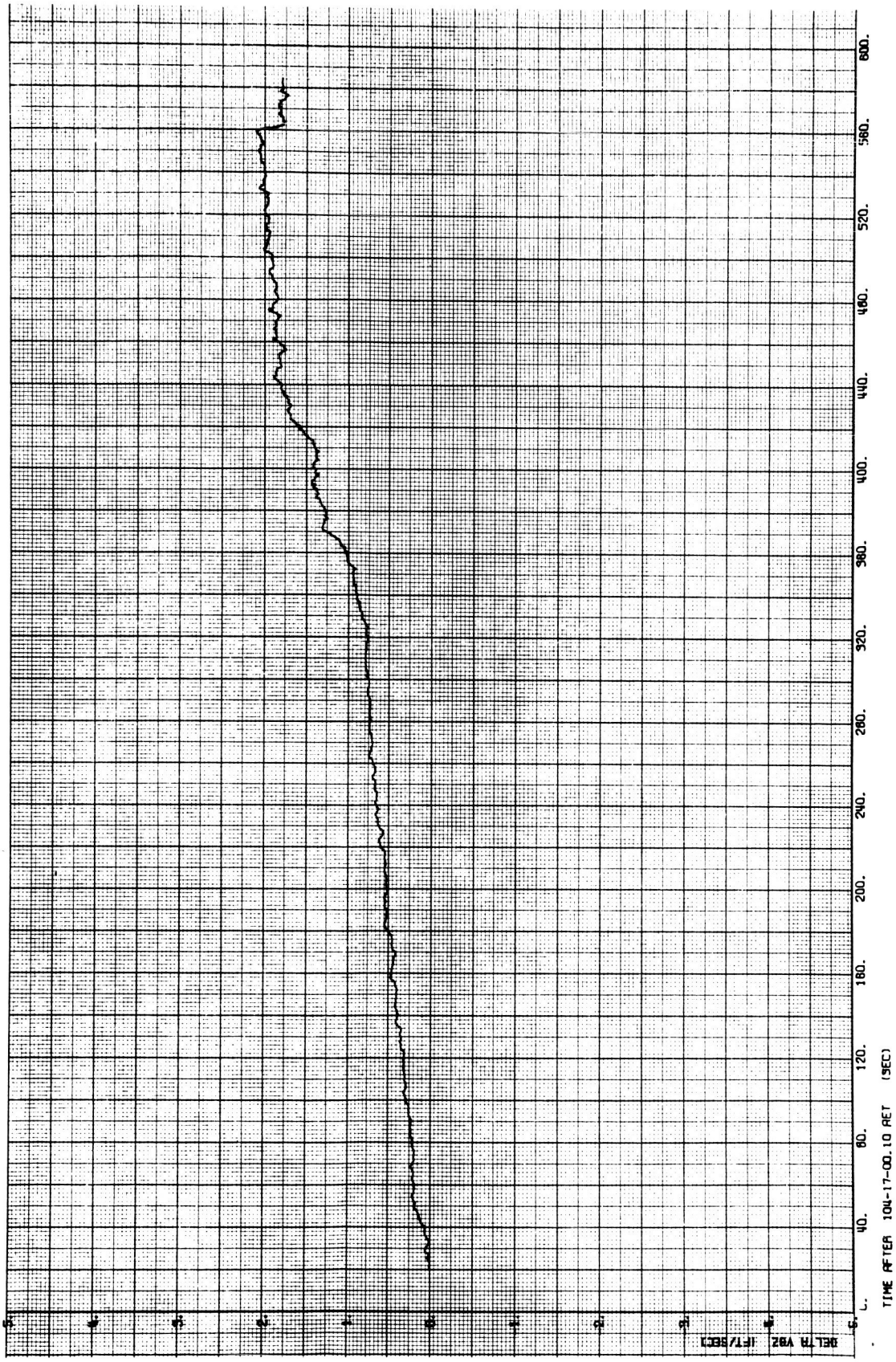


Figure 3-20. Apollo-16 LM Descent
Delta VB (AGS-PGS)

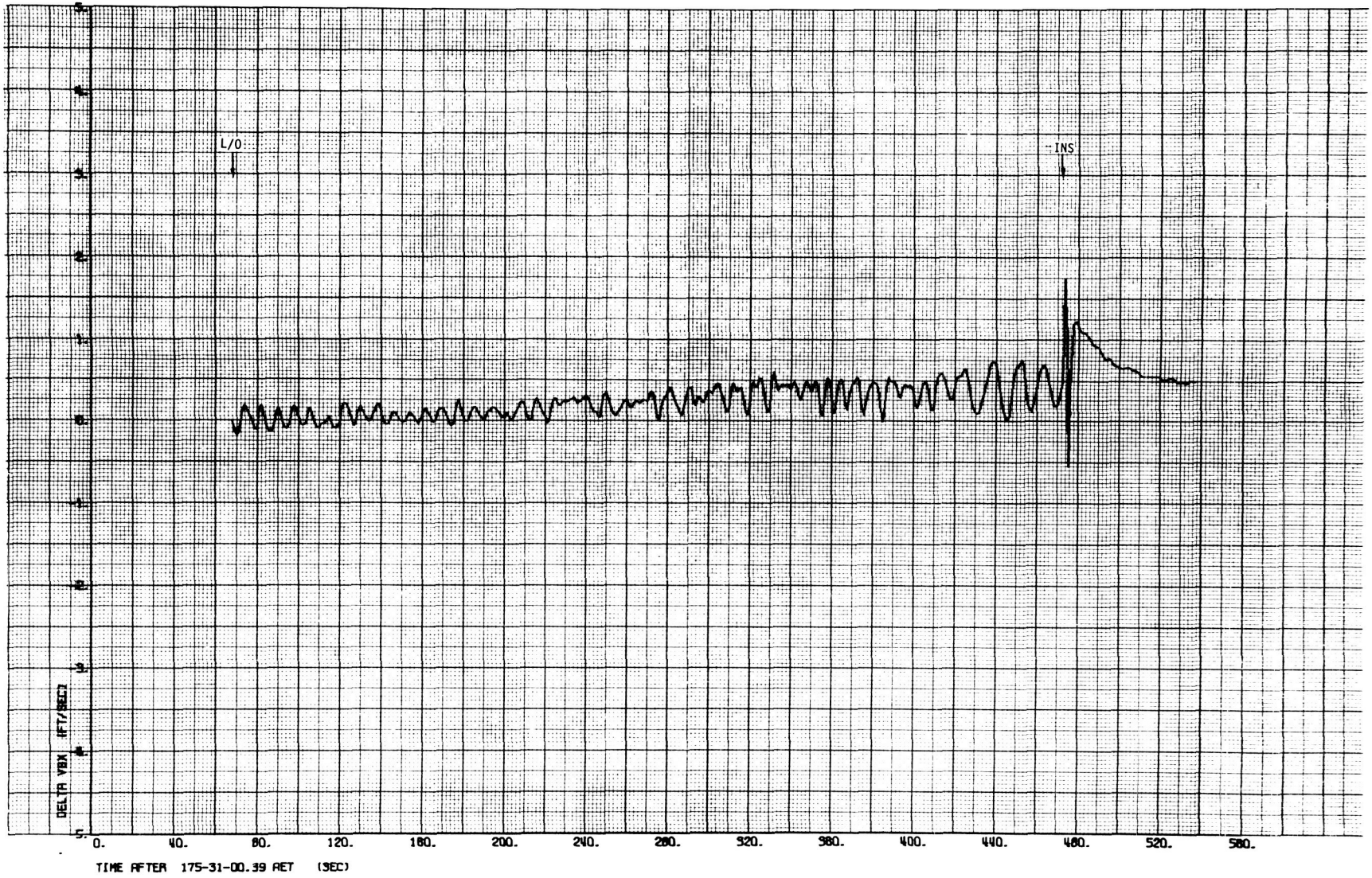


Figure 3-21. Apollo-16 LM Ascent Delta VG (AGS-PGS)

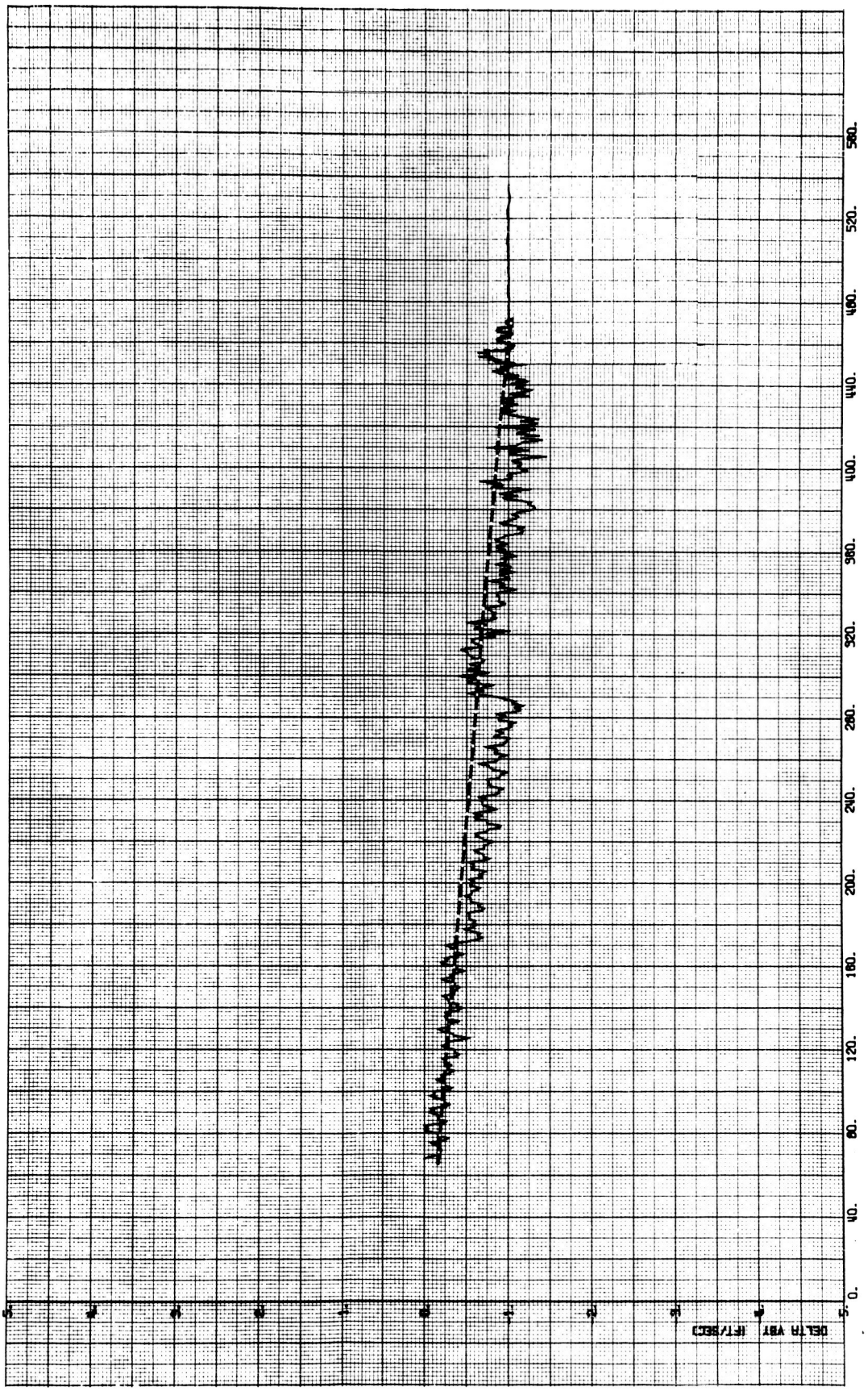


Figure 3-22. Apollo-16 LM Ascent
Delta VB (AGS-PGS)

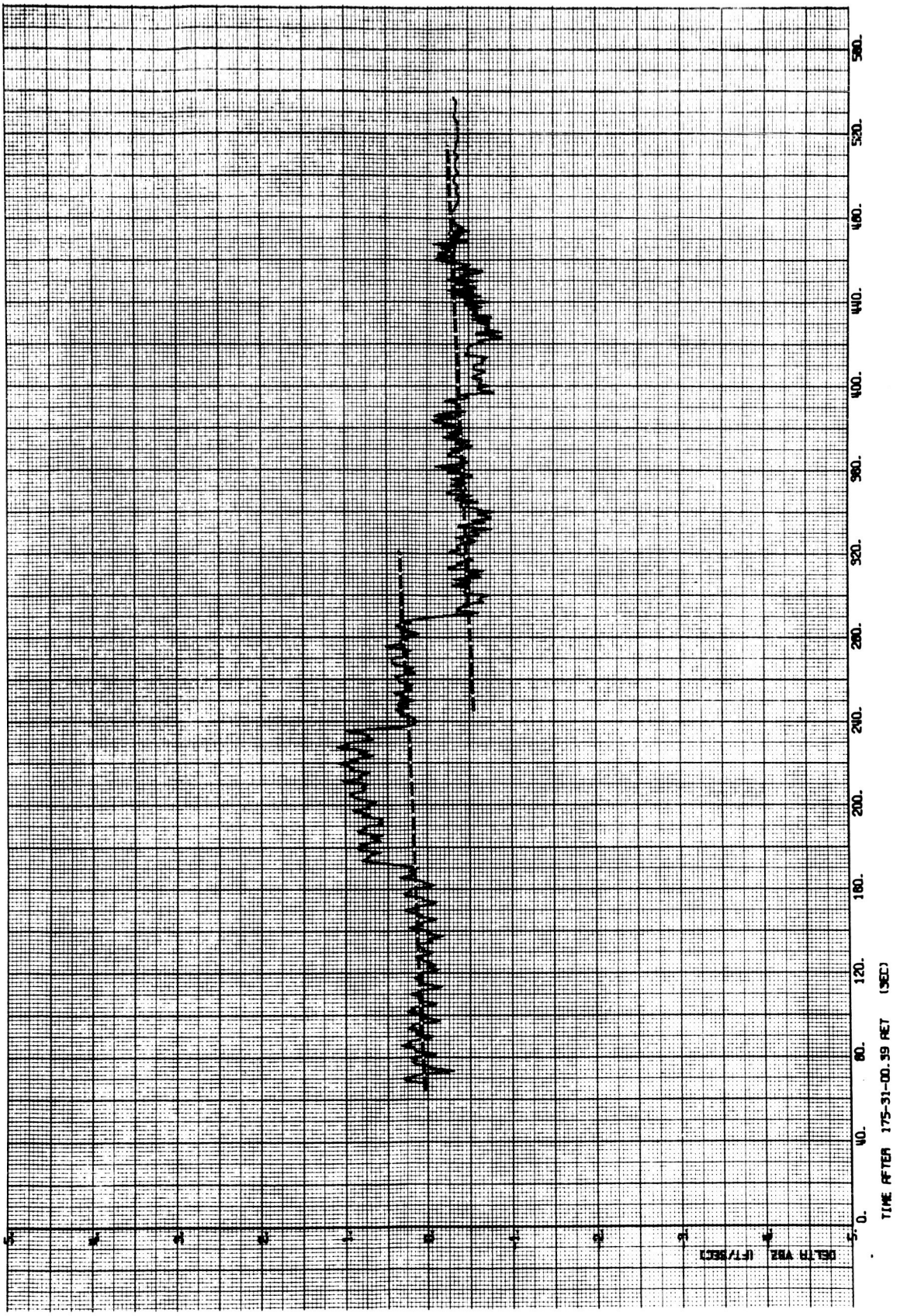


Figure 3-23. Apollo-16 LM Ascent
Delta VB (AGS-PGS)

# 4.0 LM IMU PERFORMANCE

The IMU gyro drifts and PIPA biases were particularly stable on this mission and the results are presented in Table 4.1. Only one compensation load value, ACBZ, was changed from the prelaunch load. And the ACBZ shift from 1.16 cm/sec$^2$ (the launch load) to 1.24 cm/sec$^2$ occurred between the KSC laboratory test and IMU installation in the LM. The PIPA bias shifts on the lunar surface were insignificant on this mission and the reason is partially attributable to a new shutdown procedure utilized on Apollo 16. On previous missions, no attempt was made to park the IMU in a preferred attitude which minimized bias shift. During earth testing the IMU is shutdown at an attitude with all PIPA output axes level. On Apollo 16 the IMU was parked to the preferred attitude and in addition pendulum suspension voltage was removed.

## 4.1 DESCENT ERROR FIT

IMU performance was based on assessment of a moon surface relative velocity vector at the time of touchdown which was derived from PGNCS sensed thrust velocity data independent of landing radar data. Integrating the PGNCS incremental thrust accelerations, recovered from telemetry, in a moon fixed coordinate system with origin at the landing site yielded the following moon relative velocity after touchdown.

| IMU Coordinates | Moon Relative Velocity |
|---|---|
| X | -3.8 ft/sec |
| Y | -4.6 ft/sec |
| Z | -2.7 ft/sec |

By adjusting the PGNCS sensed velocity for the following error sources, the moon relative velocity after touchdown can be reduced to near zero in all axes:

| Error Source | Error Value | Error Size Relative to Preflight Estimates |
|---|---|---|
| X accelerometer bias (ACBX) | -10 μg | 0.05 σ |
| Y accelerometer bias (ACBX) | 20 μg | 0.1 σ |
| Platform misalignment about X (MLMX) | 212 arc sec | 1.1 σ |
| Platform misalignment about Y (MLMY) | -107 arc sec | 0.5 σ |

The accelerometer bias errors were determined from free-fall data obtained before PDI and represent the difference between PIPA total bias and the LGC compensation load value.

## 4.2 ASCENT ERROR FIT

A comparison of PGNCS insertion conditions with the Powered Flight Processor (PFP) radar tracking insertion vector is shown below:

| | | Velocity-Inertial Coordinates | | |
|---|---|---|---|---|
| Source | Altitude[1] Above MLR (ft) | X (ft/sec) | Y (ft/sec) | Z (ft/sec) |
| PGNCS | 59776 | -959.48 | 0.12 | 5441.88 |
| PFP | 59750 | -959.94 | 2.19 | 5442.52 |

(1) MLR= Mean Lunar Radius = 5702395 feet.

The PGNCS vector has been adjusted for the post mission best estimate landing site and for PIPA bias error which was determined from free-flight data after the "tweak burn." The agreement is excellent when considering that the PFP tracking uncertainty is approximately 1 ft/sec and that the only required adjusting of the data to improve the match is a small platform misalignment about X. In summary, the following error model will adequately satisfy the end conditions:

| Error Source | Error Value | Error Size Relative to Preflight Estimates |
|---|---|---|
| X accelerometer bias (ACBX) | -31 μg | 0.2σ |
| Y accelerometer bias (ACBZ) | 51 μg | 0.3σ |
| Z accelerometer bias (ACBZ) | 10 μg | 0.1σ |
| Platform misalignment about X (MLMX) | -77 arc sec | 0.4σ |

Table 4-1. LM IMU PIPA Bias and Gyro Drift History

| Parameters | Preflight | | Inflight | | |
|---|---|---|---|---|---|
| | Countdown Value | Flight Load | Power-up to Surface | Surface Power-up to Liftoff | Liftoff to Rendezvous |
| | | | (a) Accelerometers | | |
| X Accelerometer | | | | | |
| Bias ($cm/sec^2$) | 1.83 | 1.84 | 1.83 | 1.84 | 1.81 |
| Y Accelerometer | | | | | |
| Bias ($cm/sec^2$) | 1.57 | 1.60 | 1.62 | 1.66 | 1.65 |
| Z Accelerometer | | | | | |
| Bias ($cm/sec^2$) | 1.23 | 1.16 | 1.24 | 1.23 | 1.25 |
| | | | (b) Gyroscopes | | |
| X Gyro | | | | | |
| Null bias drift (meru) | 0.3 | -0.3 | -1.1 | -1.41 | - |
| Y Gyro | | | | | |
| Null bias drift (meru) | -0.9 | 0.6 | 1.8 | 1.6 | - |
| Z Gyro | | | | | |
| Null bias drift (meru) | -2.3 | -2.6 | -2.0 | -3.3 | - |

# 5.0 CSM DAP OPERATION

Postflight evaluation of P20 operations during the Apollo 15 mission indicated the occurrence of large RCS jet firings for the CSM/LM configuration due to interruption of the orbital rate maneuver by state vector integration routines. To alleviate this problem, procedural changes for the Apollo 16 mission were proposed. The following were directed toward minimizing the interruption of the orbital rate maneuver:

a) Do not execute extended verbs and programs which use integration with other than current time inputs.

b) Do not uplink state vectors time tagged more than 30 minutes away from current time.

c) During SIM bay mapping camera operation (tight control required):

   1) Set SURFFLAG (V44E) to prevent two vector integration.

   2) Do not uplink vectors.

   3) Do not execute verbs or programs that integrate both vectors (e.g., V83, V85).

The most significant constraints are those precluding integration of both the CSM and LM state vectors. Integration of both state vectors results in a 20 second interruption of the orbital rate maneuver while integration of just the CSM state vector causes only a 4-second interruption.

Other modifications to the P20 Option 5 operation were implemented for the Apollo 16 mission. The wide deadbands were reduced to effect tighter attitude pointing as follows:

a) For CSM/LM configuration, 2 degree compared to 5 degree for Apollo 15.

b) For CSM alone, 3.0 degree and 2.5 degree compared to 5 degree for Apollo 15.

The 3 degree deadband was the nominal value for the Apollo 16 CSM alone configuration, but the 2.5 degree deadband was used for test purposes

since preflight simulations indicated that the average pointing would be improved for this deadband with only a small cost in RCS jet firings and propellant consumption.

For the Apollo 15 mission, the nominal spacecraft orientation for the P20 Option 5 operation was with the +X axis pointed uprange with the spacecraft rolled to a heads-down position relative to the lunar surface (Figure 5-1) which was the attitude used for Apollo 16. Apollo 15 data indicated the CSM/LM response tended toward low amplitude limit cycles located at either the plus pitch/plus yaw or minus pitch/minus yaw deadbands for this orientation. If the orbital rate interruption occurs when the limit cycle lies at the minus pitch/minus yaw deadbands, the attitude errors resulting from the interruption will cause longer than minimum impulse RCS jet firings. Conversely, if the interruption occurs at the plus pitch/plus yaw deadbands the resultant attitude errors will move back into the coast zone of the phase-plane. Therefore, for the Apollo 16 mission, an additional change was to bias the pointing attitude to insure limit cycling at the plus pitch/plus yaw deadbands for the CSM/LM configuration.

The postflight analysis was directed toward evaluating these operational changes to verify improved performance of the P20 Option 5 operations during the Apollo 16 mission.

## 5.1 CSM/LM OPERATION

The P20 Option 5 operation for the CSM/LM configuration in the 2.0 degree deadband was initiated after the DOI burn at approximately 81:12:00 AET. The P20 operation was continued through a sleep cycle until 93:08 AET. Figure 5-2 presents a time history plot of the attitude errors for the early phases of the P20 operation. The figure indicates that the pitch and yaw attitude errors migrate to the positive deadbands. A scan of the available data indicated that the CSM/LM never went to the minus pitch/minus yaw deadbands. Figure 5-3 presents an error cross-plot

for the initial phase of the CSM/LM P20 Option 5 operations. This plot, as well as the time history plot of Figure 5-2, has a discontinuity due to a short duration of free mode operation for a P52 alignment. The error cross-plot indicates two interruptions of the nominal response by state vector integrations (81:25:32.6 and 81:45:10.6 AET). The magnitudes of these effects are 0.15 degree and 0.125 degree, which are appropriate for the 4 seconds of interruption of the orbital rate maneuver. There were approximately 34 state vector integrations during the 12 hours of CSM/LM 2.0 degree P20 Option 5 operation. Data were recovered for 24 of these events and in all these cases, the CSM/LM state was near the plus pitch/plus yaw deadbands and no large RCS jet firings resulted.

Postflight analysis has verified that the deadband change from 5.0 degree to 2.0 degree for the CSM/LM configuration resulted in tighter pointing for the Sim Bay experiments. In addition procedural changes and bias pointing adopted for the Apollo 16 mission eliminated the extraneous firings resulting from interruption of the orbital rate maneuver by state vector integration and significant reduction in the number of RCS firings resulted.

Sampling of RCS jet activity during a typical orbit of quiescent P20 operation, i.e., a sleep cycle with no astronaut interruptions, indicated approximately 60 minimum impulse firings per orbit. The breakdown per axis per orbit was:

| Pitch | Yaw | Roll |
|---|---|---|
| 20 | 30 | 10 |

This is a significant improvement over Apollo 15 which exhibited approximately 100 firings per orbit, several of which were long duration firings.

## 5.2 CSM ALONE OPERATION

The problem encountered in the CSM circularization burn altered the original flight plan for the 2.5 degree and 3.0 degree deadband test of P20 Option 5. Initial use of the P20 program included only short periods

of 2.5 degree and 3.0 degree deadband operation, separated by narrow deadband (0.5 degree) P20 or inertial attitude hold. The first long duration P20 operation with a 3.0 degree deadband began at approximately 128:00:00 AET and continued essentially uninterrupted until 141:28:50 AET. The next long duration wide deadband P20 operation began at approximately 152:50:00 AET with a change to 2.5 degree deadband at 155:37:17 AET. The 2.5 degree deadband test was maintained until approximately 163:00:00 AET. The post-flight analysis concentrated on the long duration tests defined above.

The problem of extraneous, large RCS jet firings did not occur in the Apollo 15 mission for the CSM alone configuration. The gravity gradient torques for the CSM alone configuration are significantly smaller than those for the CSM/LM configuration. Therefore, the CSM alone was not held against the attitude error deadbands. Furthermore, the RCS jet authority was higher for the CSM alone vehicle and the vehicle was driven further toward zero error per minimum impulse firing. Consequently, for the majority of time, the attitude errors for the CSM alone were away from the deadbands, and the attitude error transients from the state vector integration did not result in extraneous firings. For the Apollo 16 mission, SURFLAG remained set for CSM alone operation to provide added insurance against interruption of the orbital rate maneuver by state vector integration. No bias pointing angle was used since the vehicle state generally remained away from the deadbands. Approximately fifty state vector integrations were investigated on this mission to determine whether any extraneous jet firings resulted. In all cases, the magnitude of the attitude error transient was as expected (approximately 0.12 - 0.15 degree) and none of the transients caused the vehicle state to exceed an attitude error deadband.

Figure 5-4 presents a time history plot of the attitude errors for a one-hour interval of the first long duration 3.0 degree deadband test. During the initial phase of this test period, which did include some narrow deadband modes, the roll axis exhibited two sided limit cycles (both plus and minus deadbands were exceeded). The response then settled basically into one sided limit cycles (-3.0 degree deadband) with an occasional two sided limit cycle. It is apparent from Figure 5-4 that

most of the activity, as expected, is in the roll axis with a few firings in the pitch and yaw axes. The average number of jet firings during this period was approximately 18 firings per orbit.

Figure 5-5 presents the time histories of the attitude errors for a three hour period of the first long duration 2.5 degree deadband test of P20 Option 5. Again, a period of one sided limit cycling was investigated. The average number of jet firings during this period was 22 firings per orbit.

These responses agree generally with preflight simulations which indicated the slightly higher number of jet firings for the 2.5 degree deadband versus the 3.0 degree deadband. Comparison of the average yaw and pitch pointing errors was inconclusive because of the effects of inflight venting torques. The preflight simulations did not model venting effects and indicated improved average pointing errors for the 2.5 degree deadband versus the 3.0 degree deadband. Flight data did demonstrate a greater tendency toward two sided limit cycling in the 3.0 degree deadband than predicted by the preflight simulations.

Based on the Apollo 16 inflight tests, either the 2.5 degree or 3.0 degree deadband demonstrated tighter pointing and approximately 10 percent reduction in propellant consumption for the CSM alone as compared to the Apollo 15 mission which used a 5.0 degree deadband. The preflight predictions of a lower average pointing error for the 2.5 degree deadband over the 3.0 degree deadband could not be substantiated from the flight results because of the effects of venting torques. The 2.5 degree and 3.0 degree deadband behavior essentially agreed with preflight predictions except for a higher tendency toward two sided limit cycles in the 3.0 degree deadband during the flight.

FIGURE 5-1

# VEHICLE ORIENTATION

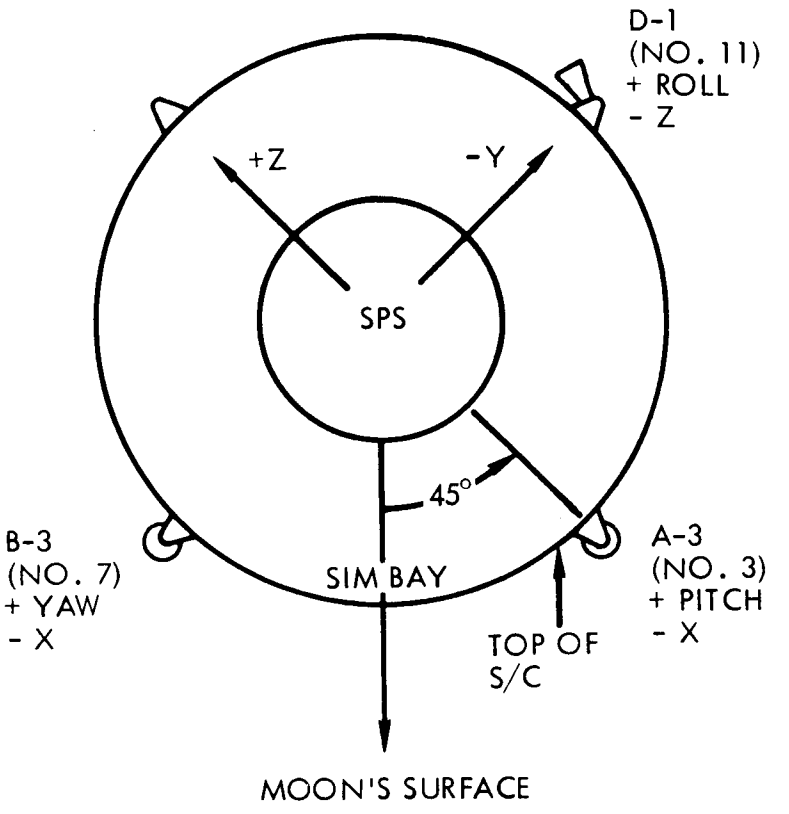


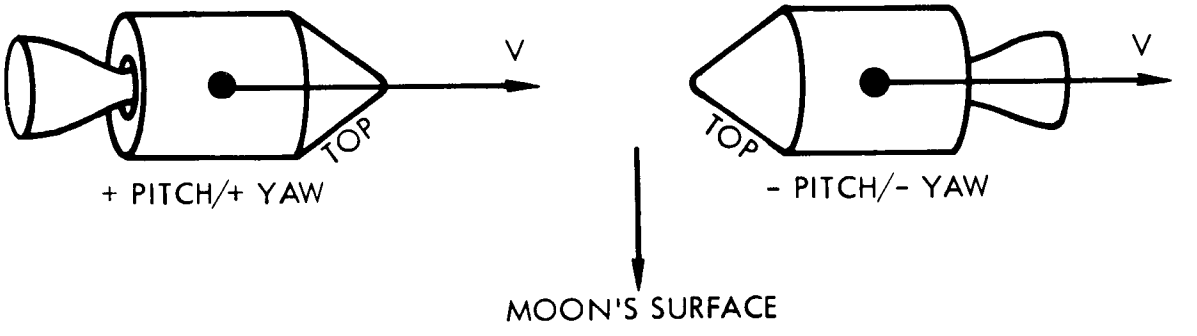

FIGURE 5-2
ATTITUDE ERROR TIME HISTORIES

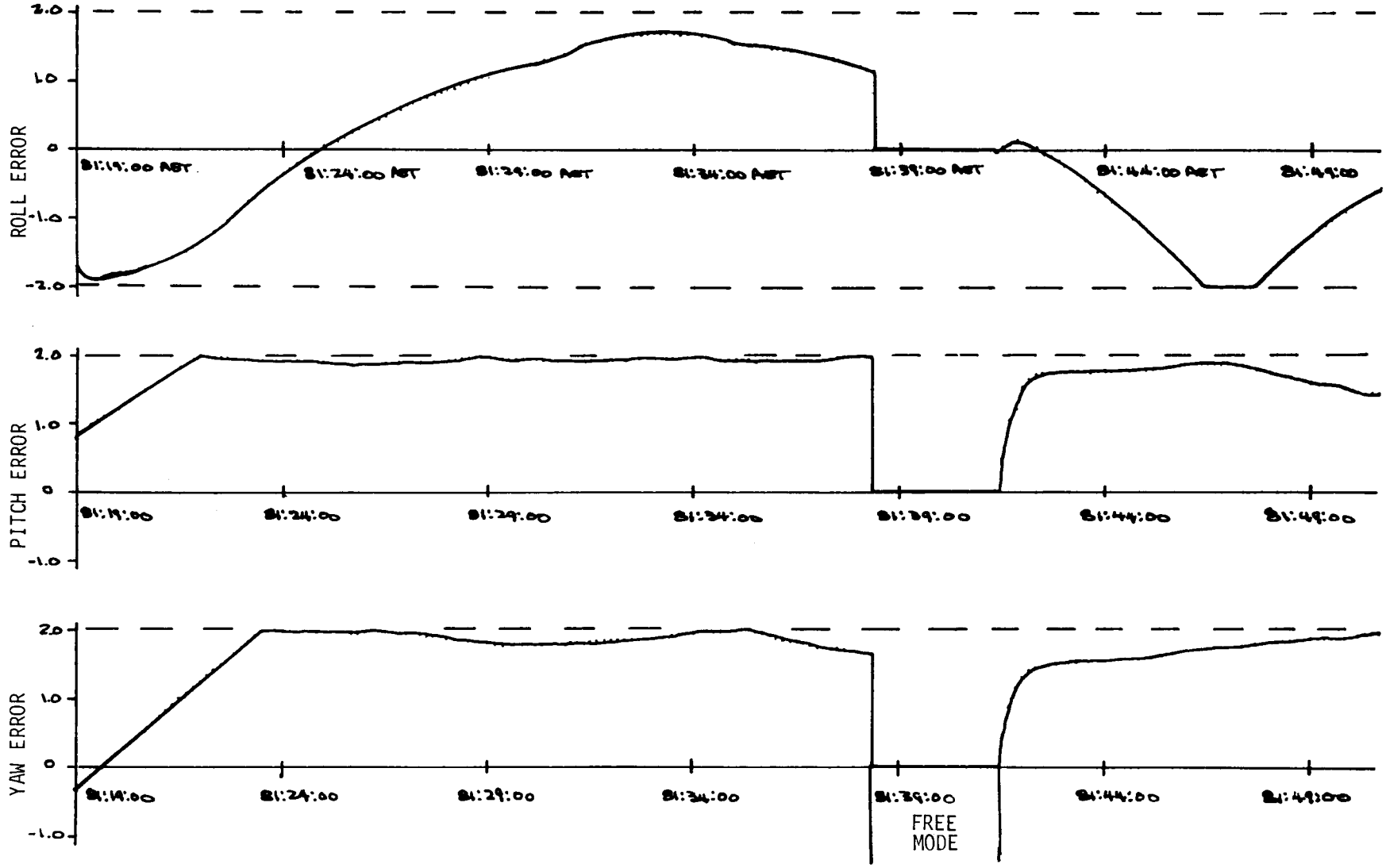

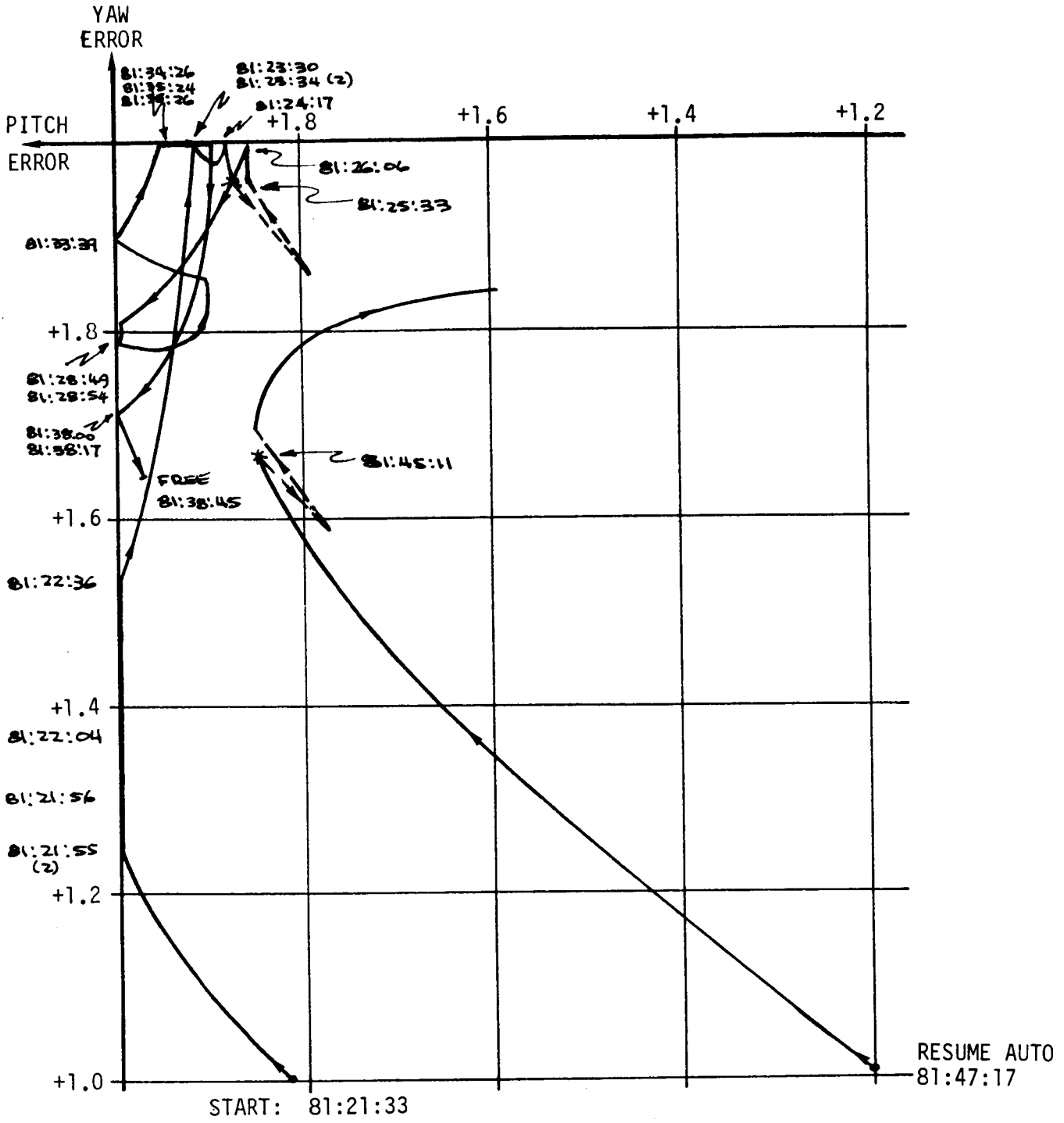


FIGURE 5-3
ATTITUDE ERROR CROSSPLOT

FIGURE 5-4
Attitude Error Time Histories
(3.0° Deadband)

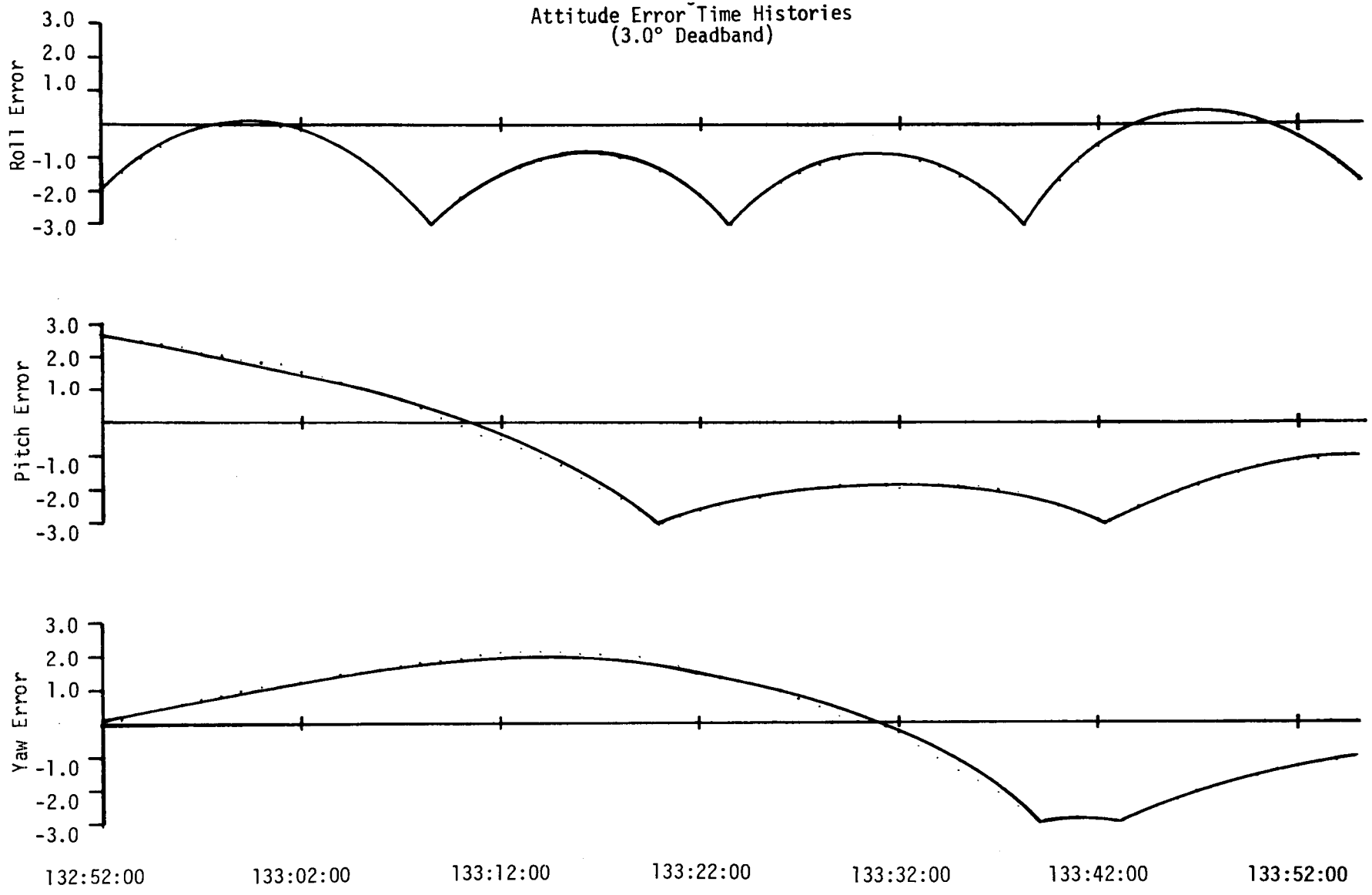

FIGURE 5-5
Attitude Error Time Histories
(2.5° Deadband)

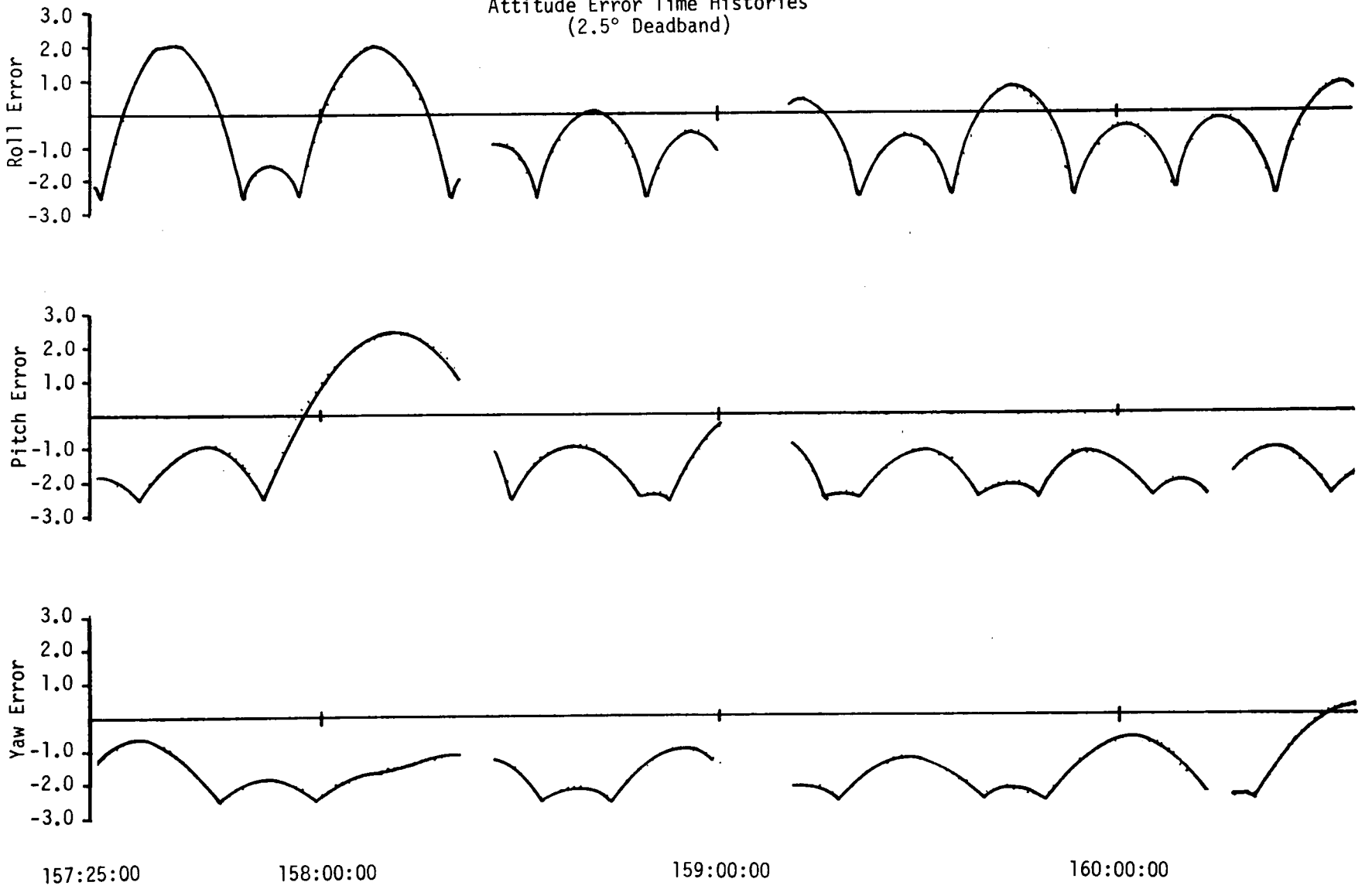

# REFERENCES